

A PSF-based approach to *Kepler*/K2 data. I. Variability within the K2 Campaign 0 star clusters M 35 and NGC 2158.*

M. Libralato^{†,2}, L. R. Bedin², D. Nardiello^{1,2}, G. Piotto^{1,2}

¹ Dipartimento di Fisica e Astronomia, Università di Padova, Vicolo dell’Osservatorio 3, Padova, I-35122, Italy

² INAF-Osservatorio Astronomico di Padova, Vicolo dell’Osservatorio 5, Padova, I-35122, Italy

Received 03 September 2015 / Accepted XX XXXXX 2015

ABSTRACT

Kepler and K2 data analysis reported in the literature is mostly based on aperture photometry. Because of *Kepler*’s large, undersampled pixels and the presence of nearby sources, aperture photometry is not always the ideal way to obtain high-precision photometry and, because of this, the data set has not been fully exploited so far. We present a new method that builds on our experience with undersampled *HST* images. The method involves a point-spread function (PSF) neighbour-subtraction and was specifically developed to exploit the huge potential offered by the K2 “super-stamps” covering the core of dense star clusters. Our test-bed targets were the NGC 2158 and M 35 regions observed during the K2 Campaign 0. We present our PSF modeling and demonstrate that, by using a high-angular-resolution input star list from the Asiago Schmidt telescope as the basis for PSF neighbour subtraction, we are able to reach magnitudes as faint as $K_p \approx 24$ with a photometric precision of 10% over 6.5 hours, even in the densest regions. At the bright end, our photometric precision reaches ~ 30 parts-per-million. Our method leads to a considerable level of improvement at the faint magnitudes ($K_p \gtrsim 15.5$) with respect to the classical aperture photometry. This improvement is more significant in crowded regions. We also extracted raw light curves of $\sim 60\,000$ stars and detrended them for systematic effects induced by spacecraft motion and other artifacts that harms K2 photometric precision. We present a list of 2133 variables.

Key words:

Instrumentation: Techniques: Image processing, Photometric / Binaries: General / Stars: Variables: General / Open clusters and associations: Individual: M 35, NGC 2158

1 INTRODUCTION

The *Kepler* observatory began science operation in May 12, 2009, with the main scientific goal of discovering exoplanet candidates transiting their host stars. The *Kepler* Input Catalog (KIC, Brown et al. 2011) includes $\sim 150\,000$ targets. The *Kepler* telescope is a defocused 0.95-/1.4-m Schmidt camera with a field of view of about 100 square degrees.

For a detailed description of the *Kepler* mission and design, see the *Kepler* technical documents web page¹ and Koch et al. (2010, and references therein). Here we provide a brief review of the relevant characteristics. On the telescope focal plane there is an array of 21 modules, each of which associated to two $2\text{k}\times 1\text{k}$ CCDs.

* Based on observation with the *Kepler* telescope and with the Schmidt 67/92 cm Telescope at the Osservatorio Astronomico di Asiago, which is part of the Osservatorio Astronomico di Padova, Istituto Nazionale di AstroFisica.

† E-mail: mattia.libralato@studenti.unipd.it

¹ <https://archive.stsci.edu/kepler/documents.html>

Each CCD is read out in two $1\text{k}\times 1\text{k}$ channels, for a total of 84 independent channels over the whole focal plane. On January 12, 2010, one module failed (MOD-3) and a second one (MOD-7) failed on February 2014. So, currently only 76 channels are operative.

The pixel scale is ~ 4 arcsec pixel⁻¹, and the deliberate defocusing causes the average point-spread function (PSF) to extend across several pixels (except in the area close to the center of the field). Even so, many features of the PSF are undersampled, even in the outskirts of the field. Knowing the exact shape of the PSF is the key for high precision photometry in crowded fields. The determination of an appropriate PSF for the *Kepler* images represents the main effort of this work.

Due to limitation in telemetry, the scientific data were downloaded once a month using a maximum data-transfer rate of approximately 550 kB/s. For this reason the *Kepler* spacecraft conducts its own pre-reduction of the data, and sends only a small portion of the exposed pixels. Around each target, a small area (a “stamp”) of various dimensions (typically a few pixels square) is read out with an integration time of 6.02 s. Every 270 exposures, the stamps are

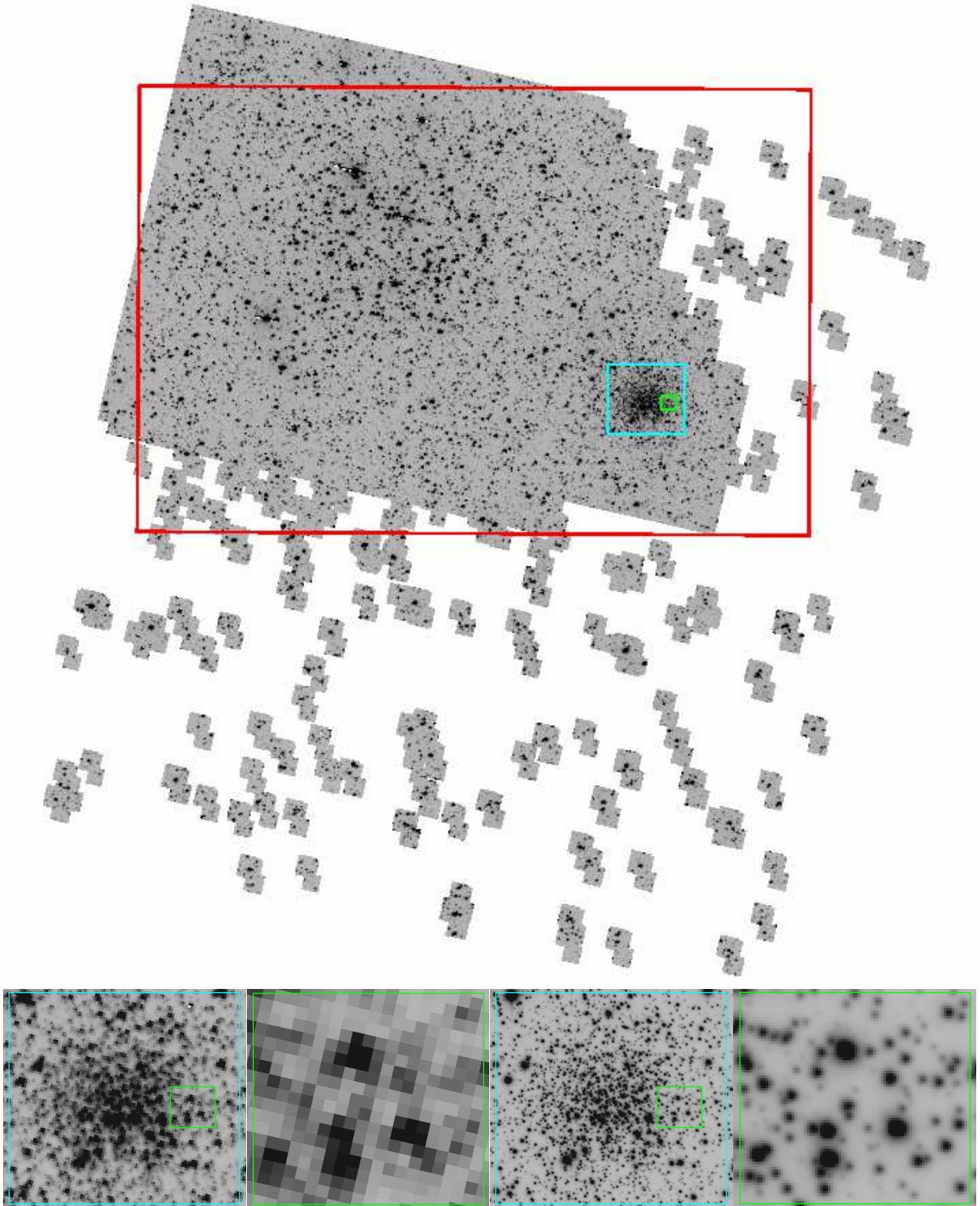


Figure 1. Field of view covered by all available *K2/C0/channel-81* exposures used in our light-curve extraction (Sect. 4). On the *Top* we show the *K2* stacked image obtained by combining 2422 exposures. The red rectangle represents the field of view of the Schmidt input list of Nardiello et al. (2015). The cyan and green boxes highlight two different zoomed-in regions around NGC 2158. In the *Bottom* row we compare these two regions in the *K2* (*Left* and *Middle-left* panels) and in the Schmidt stacked image from Nardiello et al. (2015, *Middle-right* and *Right* panels). All these images are oriented with North up and East left. It is clear that the higher resolution of the Schmidt image allows us to measure more sources than in the *K2* image, as well as to better discern close-by stars.

co-added on board to create a long-cadence stamp of about 29 minutes of total integration time; short cadences involve adding 9 exposures for a one-minute integration time. A time series of such long- or short-cadence stamps is called a target-pixel file (TPF). When several targets of interest are in a relatively small patch of sky, multiple contiguous stamps are collected together to form a so-called super-stamp. In the original *Kepler* field, two such super-stamps were taken around the stellar clusters NGC 6791 and NGC 6819.

In 2012 and 2013, the failures of two reaction wheels that were used to maintain accurate, stable spacecraft pointing, forced NASA to re-design the mission. After a period of study and evaluation, NASA approved an extension to the mission (named *Kepler*-2.0, hereafter, *K2*, Howell et al. 2014), essentially for as long as the two remaining reaction wheels continue to operate or until the fuel is exhausted.

The mission was cleverly designed to use the radiation pressure from the Sun to balance the spacecraft drift, allowing it to observe four fields per year close to the Ecliptic. Each of these fields corresponds to a so called *K2* Campaign², and can be continuously observed for \sim 75 days.

While the two functional reaction wheels control the pitch and yaw, the thruster needs to be fired every \sim 6 hours to control the roll angle of the field. This operation mode causes significantly larger jitter than in the original *Kepler* main mission. Therefore, although the *K2* data collection procedures are similar to those adopted for the original *Kepler* mission, the reduced pointing capabilities impose the adoption of 2-4 times larger target stamps. Because the *K2* stamps include 4-16 times more pixels, the number of observed targets is proportionally reduced from the \sim 150 000 targets of the original *Kepler* field to \sim 10 000-20 000 objects for the various *K2* fields. A new list of target objects is defined for each campaign: the Ecliptic Plane Input Catalog³ (hereafter, EPIC).

Despite the changes introduced in *K2* mission, several notable results have been achieved, from exoplanet discovery and characterization (e.g., Crossfield et al. 2015; Foreman-Mackey et al. 2015; Vanderburg et al. 2015) to asteroseismology (Hermes et al. 2015; Stello et al. 2015) and stellar astrophysics (Armstrong et al. 2015; Balona et al. 2015; Kraus et al. 2015; LaCourse et al. 2015).

1.1 The purpose of this study

In this study we apply our expertise on PSF photometry and astrometry on dithered and undersampled images in crowded fields (Anderson & King 2000, 2006) to extract high-precision photometry of stars in the two Galactic open clusters (OCs) M 35 and NGC 2158, which happened to lie within the *K2* Campaign 0 (C0) field.

The temporal sampling and coverage of *Kepler* and *K2* missions and their high photometric precision could be an invaluable resource for different stellar cluster fields, for example gyrochronology (Barnes 2007; Mamajek & Hillenbrand 2008; Meibom et al. 2011, 2013, 2015), stellar structure and evolution (e.g., age and Helium content from detached eclipsing binaries as done by Brogaard et al. 2011) or asteroseismology membership (Stello et al. 2011). Another interesting topic concerns exoplanets. We could improve our knowledge about the exoplanets in star clusters, in particular on how the environment (chemical composition, stellar density, dynamical in-

teraction) can affect their formation, evolution and frequency (Gilliland et al. 2000; Mochejska et al. 2004, 2006; Adams et al. 2006; Weldrake, Sackett, & Bridges 2008; Nascimbeni et al. 2012; Quinn et al. 2012, 2014; Meibom et al. 2013; Brucalassi et al. 2014).

Until now, most of the published studies based on *Kepler* and *K2* data have focused on isolated, bright objects. Focusing on *K2* data, photometry on such bright objects is well described in the literature. The main difference between the methods concern the mask determination, the stellar centroid measurement and the subsequent detrending algorithms to improve the photometric precision (for a review of the *K2* methods adopted by the different teams, see Huang et al. 2015). However, the potential scientific information on faint objects and on stars in the super-stamp crowded regions has not been completely exploited.

In this paper we intend to obtain the most accurate possible models for the *Kepler* PSFs and to use them to explore the light curves (LCs) of the sources in the densest regions that have been and will be imaged by *Kepler* and *K2*. The *Kepler* main mission includes 4 OCs (NGC 6791, NGC 6811, NGC 6819, NGC 6866); many more clusters have been and will be observed during the *K2* campaigns, which will also include the Galactic center and the Bulge (Campaign 7 and 9, respectively).

Thanks to our PSF models, for the first time on *Kepler* images, it will be possible to obtain precise photometry for stars in crowded fields, and down to $K_p \sim 24$. Having access to accurate *Kepler* PSFs and comprehensive catalogues from high-angular-resolution ground-based imaging allows us to subtract neighbours before measuring the flux of target stars, thus giving us better corrections for dilution effects that might result in under-estimates of the true radius of transiting/eclipsing objects. Indeed, the combination of PSFs and catalogues allow *all* reasonably bright sources within the stamps to be measured accurately. Finally, even without ground-based imaging, accurate PSFs, combined with aperture photometry, will allow better identification of blends. We will illustrate a few examples of mismatched variables in the EPIC catalogue, showing that the real variable is a different, much fainter source (see Sect. 7.3).

2 IMAGE RECONSTRUCTION

This pilot paper makes exclusively use of pixels within channel 81 and collected during *K2* Campaign 0, focusing on the OCs M 35 and NGC 2158. We downloaded all the *K2* TPFs, which contain the complete time series data, for both these clusters from the “Mikulski Archive for Space Telescopes” (MAST). In our approach we find it more convenient to work with reconstructed images of the entire channel, putting all saved pixels into a common reference frame, rather than working with separate stamps. This gives us a better sense of the astronomical scene and enables us to work with all pixels collected at a same epoch in a more intuitive way. We assigned a flag value to all pixels in the CCD unsaved in any stamp.

We wrote a specialized PYTHON routine to construct an image for each cadence number of the TPFs and the corresponding *Kepler* Barycentric Julian Day (KBJD) was defined as the average KBJD of all the TPFs with the same cadence number. For C0 channel 81 we thus reconstructed a total of 2422 usable images. Each channel-81 image is a 1132×1070 pixel² array. The value assigned to each pixel in each image is given by the FLUX column of the corresponding TPF. To cross-check that the reconstructed images were correct,

² <http://keplerscience.arc.nasa.gov/K2/Fields.shtml>

³ <https://archive.stsci.edu/k2/epic/search.php>

we compared them with full-frame images of the field (which were also available from the MAST).

Figure 1 gives an overview of our data set. We show the coverage and the resolution the *K2* stacked image obtained with 2422 images and the Schmidt stacked image from Nardiello et al. (2015, see Sect. 4.1 for the description of the catalogue and its usage).

3 POINT-SPREAD FUNCTION MODELING

Even taking into account the large defocusing of the *Kepler* camera, its PSFs are still undersampled. Indeed, *Kepler* PSFs are not simple 2-dimensional Gaussians, and several of the PSF’s fine-structure features are severely undersampled. If not correctly modeled, these substructures can introduce sources of systematic errors into the measurement of the positions and fluxes of the studied sources. Furthermore, if a PSF model is not sufficiently accurate, any attempted neighbour-subtraction results in spurious residuals and consequent systematic errors.

Anderson & King (2000), hereafter AK00, introduce a convenient formalism to model the PSF. Rather than model the *instrumental* PSF as it impacts the pixels, they model the *effective* pixel-convolved PSF (ePSF) in a purely empirical way using a simple look-up table formalism. Their PSF is similar to the *pixel response function* (PRF) described in Bryson et al. (2010). One of the issues that AK00 found in modeling the undersampled *Hubble Space Telescope* (HST) WFPC2 PSF is that such PSFs suffer from a degeneracy between the positions and the fluxes of the point sources. An appropriate calibration data set where stars are observed in different pixels of the detector and maps different sub-regions of the pixels is required to solve for this issue.

The AK00 approach involves taking a dithered set of exposures and empirically constructing a self-consistent set of star positions and a well-sampled PSF model that describes the distribution of light in the pixels. Such a data set was taken for *Kepler* during *Kepler*’s early commissioning phase (see Bryson et al. 2010 for a description), but unfortunately it has not yet been made available to the public (though it may be within a few months according to Thomas Barclay, private communication).

Given the urgent need for PSFs to make optimal use of the *K2* data, we decided to do the next best thing to construct an accurate set of star positions, so that properly sampled PSFs can be extracted from *Kepler* images. The main-mission *Kepler* data are not suitable for this, since they have very little dither and each star provides only one sampling of the PSF. The *K2* data are actually better for PSF reconstruction purposes, since the loss of the reaction wheels means that the spacecraft is no longer able to keep a stable pointing. Every \sim 6.5 h, a thruster jet is fired to re-center the boresight position to its nominal position. As a consequence, the stellar positions continuously change during *K2* observations, with each star sampling a variety of locations within its central few pixels. Moreover, channel 81 contains the large super-stamp covering M 35 and NGC 2158 (our main targets) with a large number of high signal-to-noise (SNR) point sources. We will see in the next sections that this mapping is not optimal, but it is the best available so far.

3.1 Initial assess of the dithered pointings

The complicated drift-and-repositioning process inherent in the *K2* data collection results in a very uneven sampling of each star in

pixel phase⁴. There are many observations at the initial phase, and few at the latter phases. We note that even with the repeated drift, a star typically samples its pixels along a line, rather than evenly across the face of a pixel, so even the achieved dither is less than ideal. In order to make the dither sampling as even as possible, we selected a subset of images (out of the 2422 exposures described in the previous section) in order to evenly map the astronomical scene across pixel phases. To do this, we used the *empirical* approach of Anderson et al. (2006) to construct an initial PSF model that was spatially constant across each detector. Such a PSF is not ideal for our ultimate purposes, but it provides better positions than a crude centroid approach and will allow us to identify a subset of images that can be used to extract the best possible PSF.

For each exposure, we made one empirical-PSF model for the entire channel because most of the stars are located in the M 35/NGC 2158 super-stamp and the spatial variability is not significant for this initial purpose. With such PSFs, we were able to measure positions and fluxes for all sources. We then built a common reference system (hereafter master frame) by cross-identifying the stars in each image. We used six-parameter linear transformations to bring the stellar positions as measured in each exposure into the reference system of the master frame. At the first iteration, the master frame was chosen using as reference one of the exposures of our sample. We then adopted a clipped-average of the single-frame positions transformed into the master frame in order to improve the definition of the master frame itself, and re-derived improved transformations. This process was iterated until the master-frame positions did not significantly change from one iteration to the next.

The transformations between each frame and the master frame allowed us to analyze the dither-pattern. In Fig. 2 we show this pattern along with its time evolution. The dither pattern was made by transforming the same pixel in each exposure into the master-frame reference system. Since the behaviour of the geometric distortion is different along the detector, the dither-pattern outline can change using a different pixel. However, for our purpose, such representation allows us to understand it anyway. It is clear that the dithering places the same star at a range of locations in its central pixels. While the dither coverage along the x axis is reasonably uniform, along the y axis the bulk of the 2422 exposures is located in a narrow area. We constructed a homogeneous mapping of the pixel-phase space (bottom-right panel of Fig. 2) as follows. We divided the pixel-phase space in a 5×5 -grid elements and, in each element, we selected by hand six exposures in order to include that sub-pixel region in our PSF construction. This was possible in almost all the cells. We ended up with 154 images out of 2422. This is a compromise between the need to have an adequate number of samplings for the ePSF, and the necessity to map the entire pixel space homogeneously, avoiding over-weighting of any sub-pixel region (by using the whole data set which is very heterogeneous).

3.2 Building the *effective*-PSF

With this subset of images, we were finally able to construct a reliable PSF model. For all exposures, we assumed the PSF to be spatially constant within our super-stamps, and to have no temporal variations. For a given star of total flux z_* located at the position

⁴ The pixel phase of a star is its location with respect to the pixel boundaries and can be expressed as the fractional part of its position: PIXEL PHASE = $x_i - \text{int}(x_i + 0.5)$.

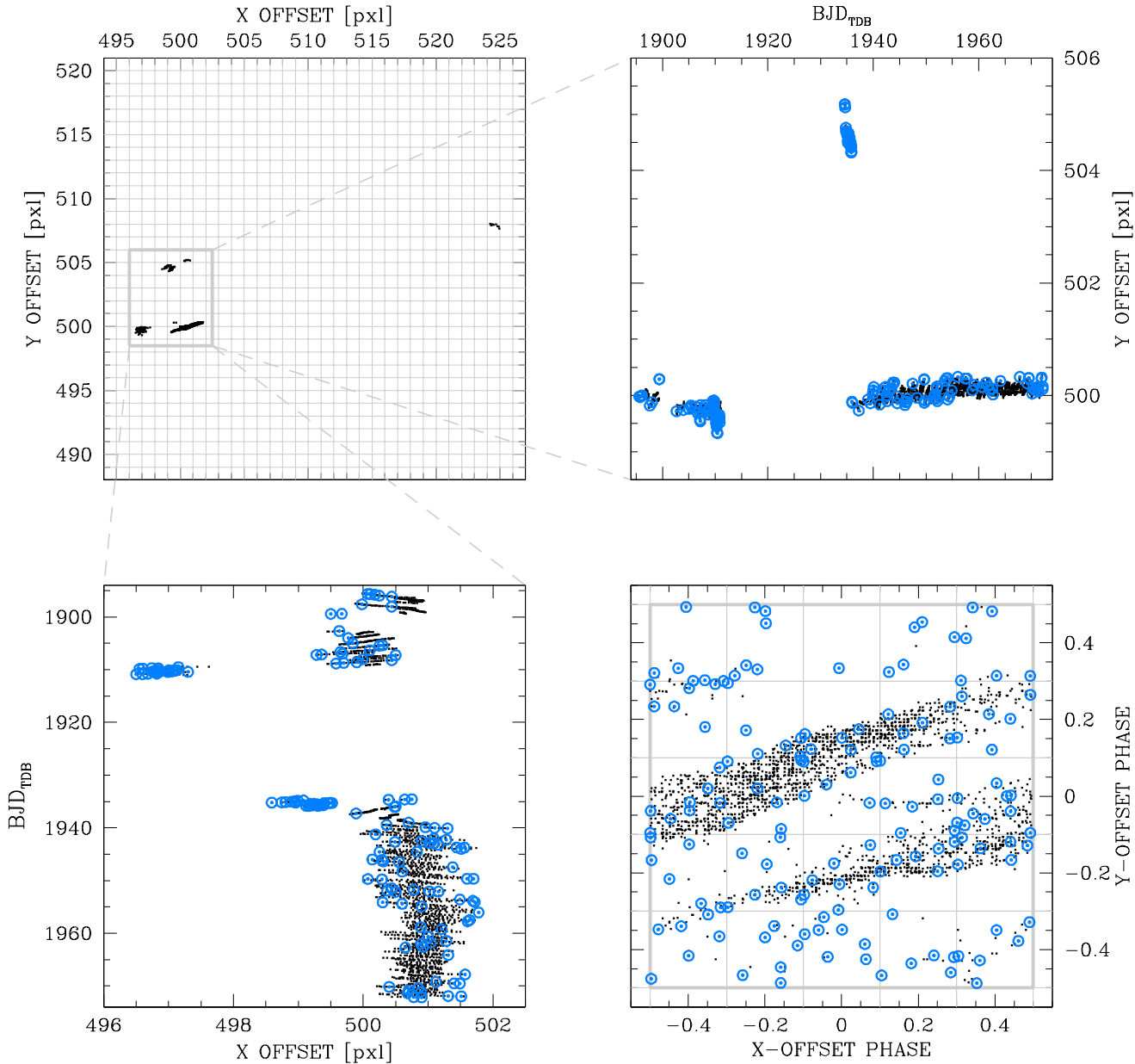


Figure 2. (Top-left): dither-pattern outline of the 2422 images used in our analysis. The gray grid represents the pixel matrix in the master-frame reference system. The thick-line gray rectangle encloses the points plotted in the Top-right and Bottom-left panels. (Top-right): y-offset variation during C0. We excluded the 10 points around (524,508) with the largest offset with respect to the average value to better show the time variation of the y-offset. The azure points are those images used for the ePSF modeling (see text). (Bottom-left): as on Top-right but for the x offsets. (Bottom-right): dither-pattern pixel phase. The center of the pixel (dark gray square) is located at (0,0). The pixel was divided into a 5x5-grid (thin gray lines) elements and, in each such element, we selected six images (when possible) to map that sub-pixel region as homogeneously as possible.

(x_*, y_*) , the value of a given pixel $P_{i,j}$ close to such star is defined as:

$$P_{i,j} = z_* \cdot \psi(i - x_*, j - y_*) + s_* ,$$

where s_* is the local sky background and $\psi(\Delta x, \Delta y)$ is the PSF, defined as the fraction of light that would be recorded by a pixel offset by $(\Delta x, \Delta y) = (i - x_*, j - y_*)$ from the center of the star. By fitting the PSF to an array of pixels for each star in each exposure, we can estimate its x_* , y_* and z_* for each observation of each star. The equation to be used to solve for the PSF can be obtained by

inverting the above equation:

$$\psi(\Delta x, \Delta y) = \frac{P_{i,j} - s_*}{z_*} .$$

With knowledge of the flux and position of each star in each exposure, each pixel in its vicinity constitutes a sampling of the PSF at one point in its two-dimensional domain. The many images of stars, each centered at a different location within its central pixel, give us a great number of point-samplings and enable us to construct a reliable ePSF model. This is described in detail in AK00. Here, we just provide a brief overview of the key points:

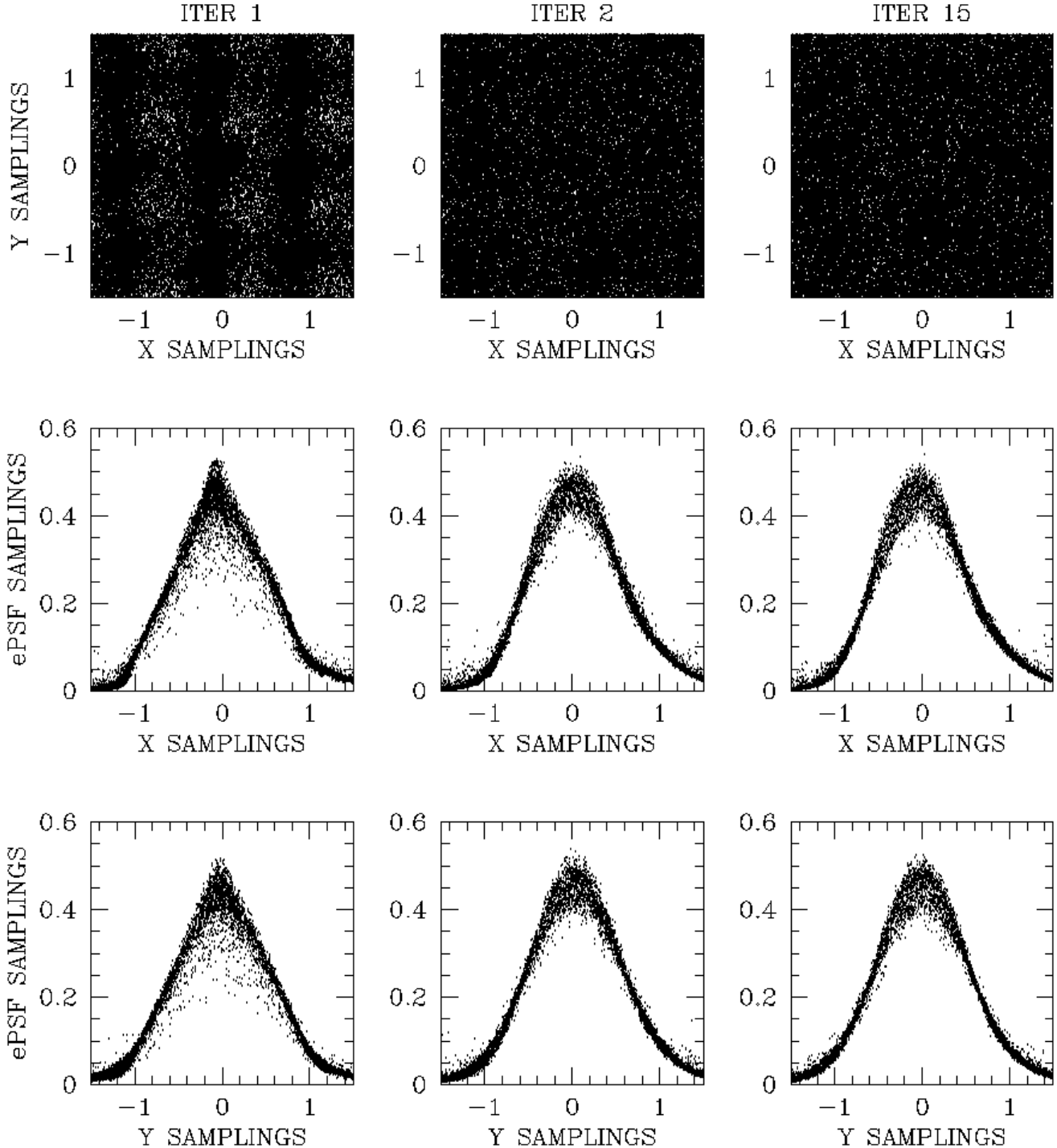


Figure 3. Effective-PSF samplings at the first (Left column), second (Middle column) and last (Right column) iteration. On the Top-row panels we show the location of the estimated value of the PSF with respect to the center of the stars, placed at (0,0). At the beginning the star position was computed using the photocenter. From the second iteration, the sampling becomes more uniform. On the Middle- and Bottom-row panels we show the ePSF profile along the x and y axes for a thin slice with $|\Delta y| < 0.01$ and $|\Delta x| < 0.01$, respectively. In all panels we plotted only 10% of the available points, for clarity.

- We made a common master frame by cross-identifying bright, isolated⁵ stars in each image and computing their clipped-averaged

positions and flux. On average, we have 650 good stars per exposure to use.

⁵ The adjective “isolated” should be considered in a relative way. Within a 1×1 -pixel square on a $K2$ exposure there could be more than one star, as

we will see in the Fig. 21. Therefore by “isolated” we mean that, in the $K2$ image, there are not other obvious stars close to the target.

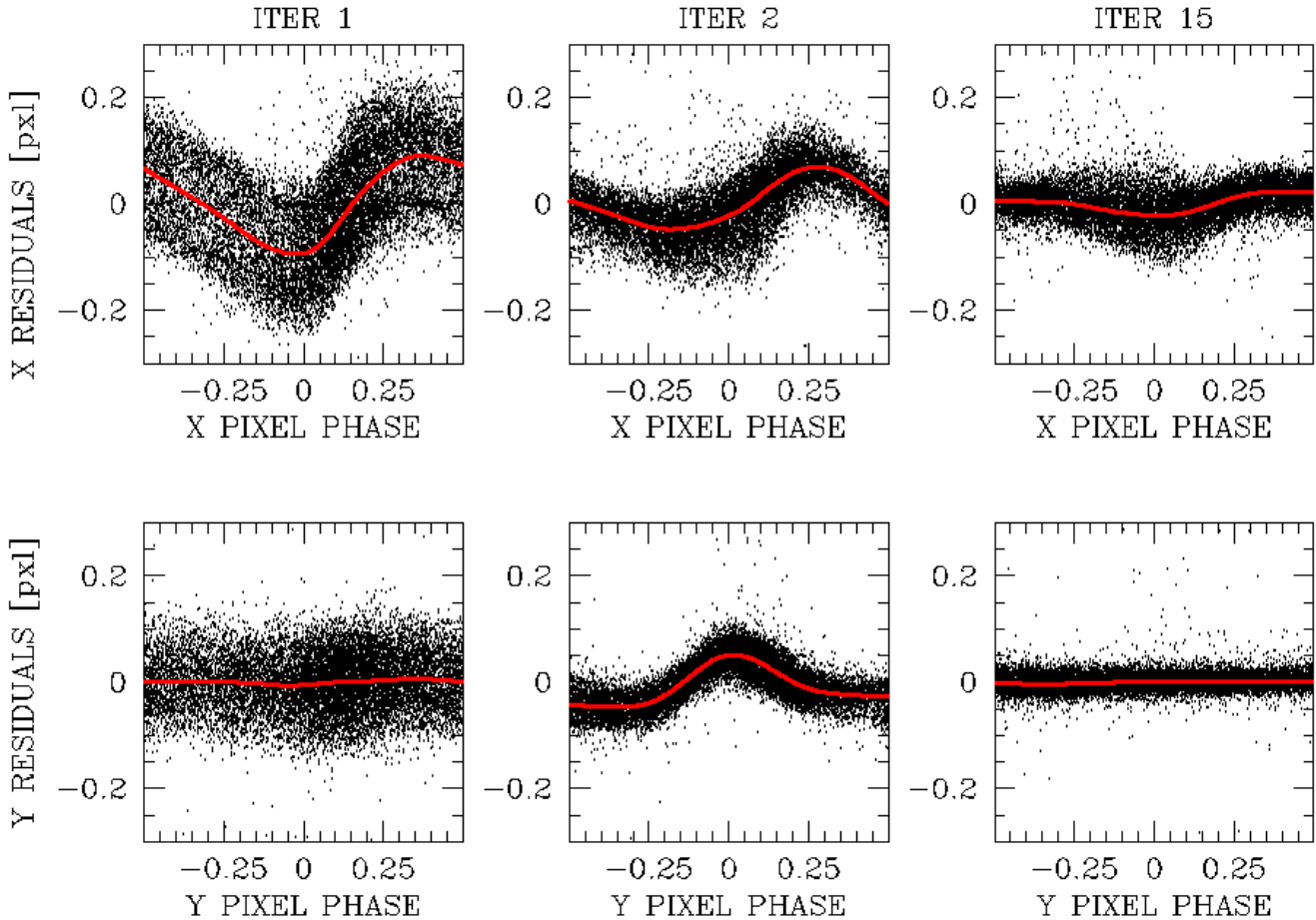


Figure 4. Pixel-phase errors progression. On the *Left* column we show the first, in the *Middle* column the second and in the *Right* column the last iteration of the ePSF modeling. In the *Top* row we show the pixel-phase errors along the x axes, in the *Bottom* row the errors along the y axes. As in Fig. 3, we plotted only 10% of the points.

- We transformed these average master-frame positions back into the frame of each image in order to place the samplings more accurately within the PSF domain (since each measure is an average of 154 images).
- We converted each pixel value in the vicinity of a given star in a given image into an ePSF sampling, and modeled the variation of the PSF across its 2-dimensional domain. We have on average 650 reliable stars per exposure, for a total of 10^5 samplings.
- The available ePSF was used to measure an improved position and flux for the stars in each image.

The whole procedure was iterated fifteen times, after which we noticed that the overall improvements were negligible (i.e., the pixel-phase errors did not change from one iteration to the next). The final ePSF was a 21×21 array of points that maps the 5×5 -pixel region around a star (as in AK00, our ePSF model was supersampled by a factor 4).

In Fig. 3 and 4, we show the result of our procedure. At the beginning, the ePSF sampling is not homogeneous and the shape of the ePSF is not well constrained. Even in the second iteration, the sampling began to improve and the ePSF became smoother. The same behavior can be seen in the pixel-phase errors. Note that the pixel-phase errors appear to be behaved along the y axes rather than the x axes. However, it is not clear whether the available pixel-phase sampling simply allows us to see the errors in x better than

those in y . Again, when the *Kepler* PSF-characterization data set becomes public, it will allow for a much better characterization and verification of the PSF.

3.2.1 Comparison with Kepler-main-mission PRFs

Following a suggestion by the referee, we investigated whether our *K2/C0* ePSF is broader than the *Kepler*-main-mission PRF (Bryson et al. 2010). The broadening is expected because of the *K2* pointing jitters larger than those in the main mission.

We measured the full-width half-maximum (FWHM) of the five channel-81 PRFs (one for each corner and one for the central region of the CCD) and that of our average ePSF along different directions. In Fig. 5, we show a contour representation of our ePSF and the central PRF of Bryson et al. (2010). The ePSF size in these representation is the same as for the PRF (in *Kepler* pixels). Our ePSF is limited to a small region around the center and do not model the ePSF wings, as the crowding in the studied super-stamp does not allow the modeling of the ePSF wings. In the right panel of Fig. 5 we show the median FWHM values for the PRFs/ePSF. We found that our *K2/C0* ePSF is broader than the *Kepler*-main-mission PRFs.

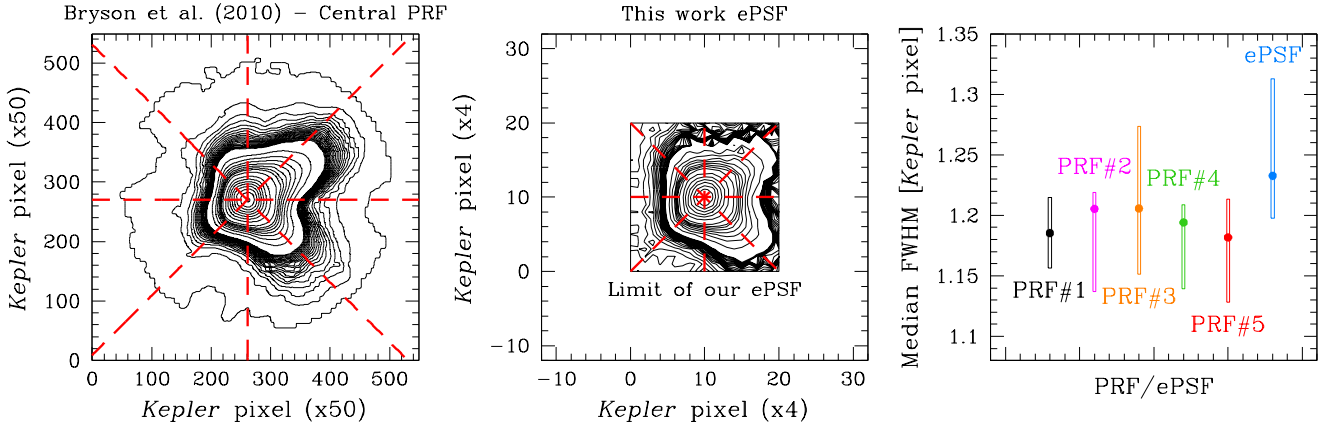


Figure 5. FWHM analysis. In the *Left* and *Middle* panels, we show a contour representation of channel-81 central PRF and our average ePSF, respectively. The red dashed lines show the direction along which we measured the FWHM ($-45, 0, 45$, and 90 degrees). The PRF and the ePSF are plot with their original supersampling factor (50 and 4, respectively) but their size in the images are the same (in real *Kepler* pixels). It is clear that our ePSF is limited to the center part, due to the data set used that was not designed to model it. In the *Right* panel, we show in different colours the median of these FWHM values for the five PRFs (black, magenta, orange, green and red) and for our *K2/C0* ePSF (azure). The rectangle around each point shows the minimum-to-maximum range of the FWHM values along the considered directions.

3.3 Perturbed ePSF

The basic assumption of the original AK00 method is that the ePSF is constant in time and identical for all the images. This is of course an ideal condition and—at some level—it is never the case; surely not for the *HST* nor for any other instrument we have used. There are also other subtle effects. The selection of a uniformly-distributed subsample of images in pixel-phase space could have introduced some biases. For example, some of the dither pointings in the less-populated regions of the pixel-phase space could have been taken while the telescope was still in motion, resulting in a more “trailed” ePSF than the average ePSF. In any case, as a working hypothesis, and having detected no obvious trailed images in the subsample that we selected for the ePSF determination, we proceeded under the approximation that these effects are not larger than the general, ePSF variations as a function of time. Indeed, the shape of the *Kepler* ePSF clearly changes over time, as one can infer in Fig. 3 from the vertical broadening of the ePSF around the center (rightmost middle and bottom panels).

Figure 6 illustrates the temporal variation of the PSF. We colour-coded the samplings of the final ePSF (top panels) according to the epoch of observation (see bottom panel). There are clear trends that are not simply monotonic.

In order to suppress as much as possible the impact of the temporal dependencies of the ePSF we introduced a perturbation of the average ePSF. This perturbation of the ePSF was first described in Anderson & King (2006), and can be summarized as follows. In each image, we fit and subtracted the current ePSF model to high SNR stars. We then modeled (with a look-up table) the normalized residuals of these ePSF fits and added these tabulated residuals to the initial ePSF to obtain an improved ePSF model (for a more recent application and a detailed description of the method see Bellini et al. 2014).

In Fig. 7 we show an example of the time-variation adjustments of the average ePSF for two images. The improvements in position and flux of the perturbed ePSFs over a constant ePSF for all the 2422 images are quantified in Fig. 8. We measured position and flux of all sources in each exposure with and without perturbing the ePSF. The PSF-fit process (a least-square fit) is achieved with

a program similar to the `img2xym_WFI` described in Anderson et al. (2006) that measure all sources, from the brightest to the faintest (up to a minimum-detection threshold set by the user) objects, in seven iterations. From the second iteration ahead, the fitting procedure is also performed on neighbour-subtracted images, in order to converge on reliable positions and fluxes for close-by objects. We then made two master frames, one for each of the two different approaches, by cross-identifying the stars in each of our 2422 images. We computed the 3σ -clipped median value of the following quantities: QFIT⁶, the 1D positional rms, and the photometric rms. These values were calculated in 1-magnitude bins and, for an appropriate comparison, we used the same set of stars for the two samples. In most cases, we found that the difference between the use of perturbed or unperturbed ePSF is not negligible. Using the perturbed rather than the average ePSF to measure position and flux of a star in an image improves the PSF fit because the former is a representation of a star in that particular image, while the latter is the representation of a star averaged on the entire C0.

In the following, we assume that the spatial variation of the ePSF across the super-stamp region in channel-81 detector where NGC 2158 and M 35 are imaged is negligible, therefore we will use only one ePSF model per image. A substantial improvement to the ePSF will be achieved when the PSF characterization data are made available, so that we can properly account for the spatial variability.

4 PHOTOMETRY IN *K2* RECONSTRUCTED IMAGES

The main purpose of this effort is to extract precise photometry from main-mission and *K2*-mission pixel data for sources in crowded fields and at the faintest end. These two issues are very closely related, since each $4'' \times 4''$ pixel includes many faint sources that we need to take into account. Because of this crowding, classical aperture photometry has major obvious limitations.

⁶ The QFIT represents the absolute fractional error in the PSF-model fit to the star (Anderson et al. 2008). The lower the QFIT, the better the PSF fit.

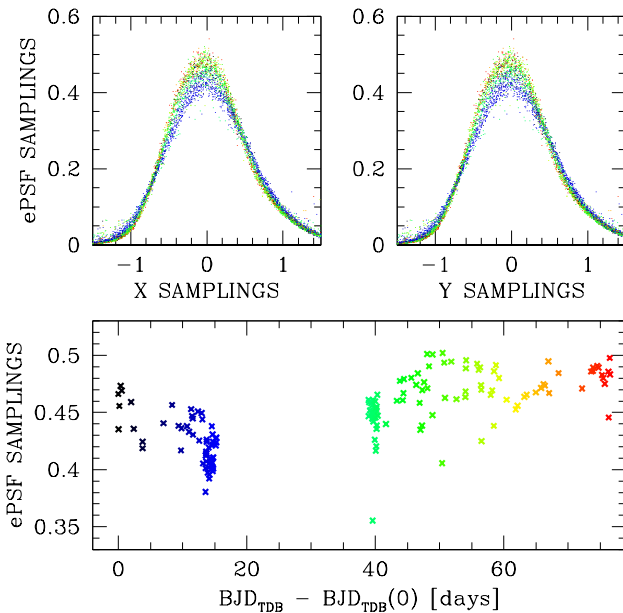


Figure 6. Time variation of the ePSF shape in the 154 images we used for the modeling. In the *Bottom* panel, the central-peak value of the ePSF (interpolated from the samplings) as a function of the time interval relative to the first-image epoch. In the *Top-left* and *Top-right* panels we show the ePSF samplings as in the *Right* column of Fig. 3, using the same colour-codes for the time of image acquisition.

Different authors showed that photometry on neighbour-subtracted images leads, on average, to a better photometric precision than on the original images (see, e.g., Montalto et al. 2007 and reference therein). By subtracting a star’s neighbours before measuring its flux, it is possible to avoid including (or at least to reduce the impact of) light that could contaminate the true flux of the target. The knowledge of positions and flux of all sources in the field is therefore fundamental to our approach.

In order to obtain the best photometric precision with *K2* data, we used the same method as described in Nardiello et al. (2015) to which we refer for a more detailed description. This method makes use of accurate PSF models for each exposure and of a (ground-based) input list to disentangle from the flux of a given star the contribution of its close-by sources. The more complete the input list with all detectable objects in the field, the better will be the final result of the method. A corollary is also that the transformations of the input-list positions and fluxes into the individual-exposure reference system need to be known with high accuracy, as well as the PSF, in order to subtract the neighbours as well as possible. In the following we provide the adopted key ingredients.

4.1 The Asiago Input Catalogue (AIC)

Our input list is described in great detail in Nardiello et al. (2015). It comes from a set of white-light (i.e., filterless) observations collected at the Asiago Schmidt telescope. It includes 75 935 objects. At variance with Nardiello et al., we used all stars measured in white light, and not only those found in both white-light and *R*-filter lists (see Sect. 3.5 of their paper). Hereafter, we will refer to this catalogue as the *Asiago Input Catalogue*, or AIC, which is

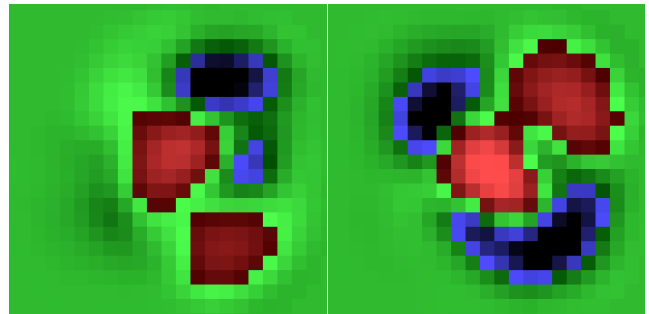


Figure 7. Difference between the average ePSF and the perturbed ePSF for an image at the beginning (*Left*) and at the end (*Right*) of Campaign 0. In these two examples, the variation ranges between ~ -0.5 per cent (blue colour) and ~ 1.4 per cent (red colour) of the total flux.

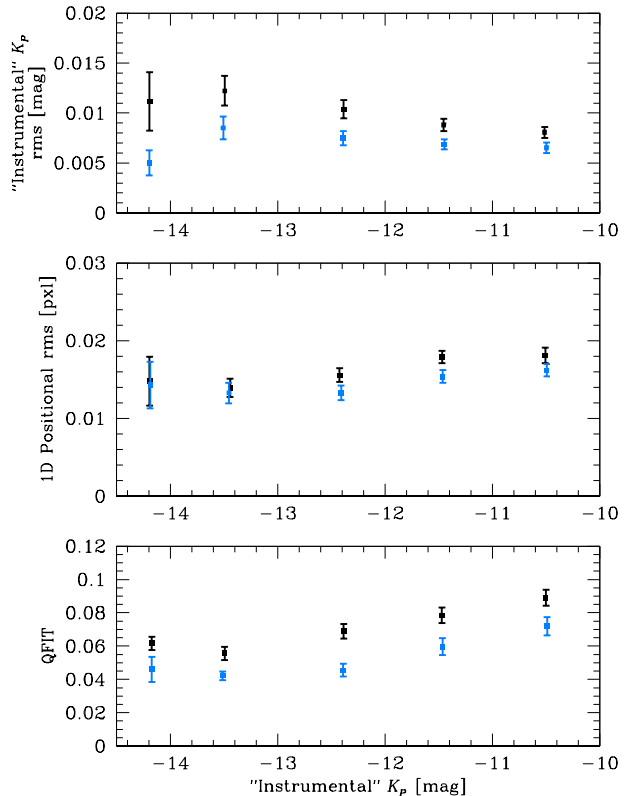


Figure 8. QFIT (*Bottom*), 1D positional rms (*Middle*) and photometric rms (*Top*) as a function of the “instrumental” magnitude of the master frame with (blue points) and without (black points) perturbing the average ePSF to account for the time-dependent variations. Each point represents the median value in 1-magnitude bins. The error bars represents the 68.27th percentile of the distribution around the median value divided by \sqrt{N} , with N number of points. The instrumental magnitude in each single catalogue is defined as $-2.5 \times \log(\sum \text{counts})$, where $\sum \text{counts}$ is the sum of the total counts under the fitted PSF. Since we used the column FLUX while building the full-frame channel images, these counts are actually fluxes (for this reason we used the double quotes in the label). Hereafter, we will omit the double quotes in the text.

available at the “Exoplanet and Stellar Population Group” (ESPG) website⁷.

The AIC was constructed by measuring the position and flux of each source found in the Schmidt stacked image via PSF fitting. This input list was then transformed into the photometric system of a reference image (among those of the Schmidt data set). The catalogue was purged for various artifacts, such as PSF bumps and fake detections along the bleeding columns. The purging is not perfect and it is a compromise between excluding true, faint stars around bright objects, and including artifacts in the catalogue. Of the 75 935 sources included in the input list, ~77% could be measured reasonably well with the *K2* data set.

The stacked Schmidt image has higher angular resolution than the *Kepler/K2* images, allowing us to locate faint sources whose flux could pollute the pixels of a nearby star. The relative astrometric accuracy of the AIC is also sufficiently accurate to allow us to pinpoint a star in any given *K2* image with an accuracy down to about 20 mas (0.005 *Kepler* pixel). Details about the absolute astrometry, the stacked images, and other information of the AIC can be found in Nardiello et al. (2015).

4.2 Photometry with and without neighbours

The procedure for LC extraction is the same as in Nardiello et al. (2015) and can be summarized as follows. For each star in the AIC, hereafter “target star”, we computed six-parameter, local linear transformations to transform the AIC position of the target into that of each individual *K2* image. In order to compute the coefficients of the transformations, we used only bright, unsaturated, well-measured target’s neighbours within a radius of 100 pixels (target star excluded). If there were not at least 10 neighbour stars within such radius, we increased the searching area progressively, out to the whole field. Local transformations were used to minimize the effect of the geometric distortion, since it does not vary significantly on small spatial scales.

These reference stars were also used to transform the AIC white-light magnitude of the target into the corresponding instrumental *K2* magnitude in each given exposure. The AIC magnitudes in white light and our K_p instrumental magnitudes are obtained from instruments with a rather similar total-transmission curve and, as a first approximation, we can safely use a simple zero-point as photometric transformation between AIC and *K2* photometric systems.

We extracted the photometry from the original and from the neighbour-subtracted *K2* images. The neighbour-subtracted images were created by subtracting from the original images the flux-scaled perturbed ePSF of all AIC sources within a radius of 35 *Kepler* pixels (~2.3 arcmin) from the target star. We postpone the discussion about the quantitative improvements in the photometry by using neighbour-subtracted images instead of the original images to Sect. 7.1.

On the neighbour-subtracted images, the target flux of each AIC object was measured using aperture photometry with four aperture sizes (1-, 3-, 5- and 10-pixel radius) and using ePSF-fit photometry. On the original images, we used only 3-pixel-aperture and ePSF-fit photometry. These fluxes were stored in a LC file, which also contains other information such as the KBJD.

5 PHOTOMETRIC CALIBRATION INTO THE K_p SYSTEM

In order to calibrate our the instrumental magnitudes we extracted from the individual *K2* exposures to the *Kepler* Magnitude System (K_p), we determined and applied a simple local zero-point. For each photometric approach (1-, 3-, 5-, 10-pixel aperture and PSF), we made a catalogue with absolute positions from the AIC and with magnitudes obtained from 3σ -clipped median values of the *K2* instrumental magnitudes as measured in each LC (when available). We then cross-matched these catalogues with the EPIC obtained from the MAST archive. We computed the zero points as the 3σ -clipped median value of the difference between our magnitudes and the EPIC K_p magnitudes. We used only those bright, unsaturated stars that in our catalogue are within three magnitudes from the saturation and for which the K_p magnitude in the EPIC was obtained from ‘gri’ photometry. We chose this specific photometric method among the different methods adopted to compute the K_p magnitude in the EPIC due to the larger number of sources in common between this EPIC subsample and our well-measured-star sample. As in Aigrain et al. (2015) and Lund et al. (2015), the zero-points of our photometric methods we found are between 24.7 (1-pixel aperture) and 25.3 (the other photometric methods).

6 DETRENDING OF *K2* LIGHT CURVES

The unstable spacecraft pointing results in a well-defined motion of the stars across the pixel grid. A combination of intra- and inter-pixel sensitivity variation leads to a correlation between this motion and the “raw” flux of each star that must be corrected in order to increase the *K2* photometric accuracy and precision. Different methods have been developed to correct such systematic effect, e.g., the self-flat-fielding approach of Vanderburg & Johnson (2014), the Gaussian process of Aigrain et al. (2015) or the simultaneous fit for all systematics of Foreman-Mackey et al. (2015).

In order to detrend the LCs from the drift-induced effects, we took into account all usable channel-81 exposures collected during the entirety of C0, including those taken during the first part of the campaign, when the fine guiding was still in progress (which caused the stars to be shifted by up to 20 pixels from their average position, see Fig. 2). This is important, since the number of points to be used for the detrending increases, and it could also be useful to detect variable stars with periods of ~35 days (the duration of the C0 after the second safe mode). Briefly, our correction was performed by making a look-up table of corrections and applying it with simple bi-linear interpolation.

An overview of our detrending approach is shown in Fig. 9. For each target star, we made a model of the raw LC trend, normalized by its median flux (panel a), by applying a running-average filter with a window of ~10 hours. The model (panel b) was then subtracted from the raw LC with the aim of removing the intrinsic stellar variability. In this way, the model-subtracted LC (panel c) reflects the systematic effect originated from the motion of the spacecraft. The window size of the running-average filter was chosen as a compromise between our attempt of avoiding the removal of the positional trend and still being able to model short-period variables.

Each pixel into which a given star fell during the motion was divided into an array of 20×20 square elements and, in each such element, we computed the 3.5σ -clipped median of the model-subtracted LC flux. The grid is sketched in panel (f) and (g) of

⁷ <http://groups.dfa.unipd.it/ESPG/M35NGC2158.html>

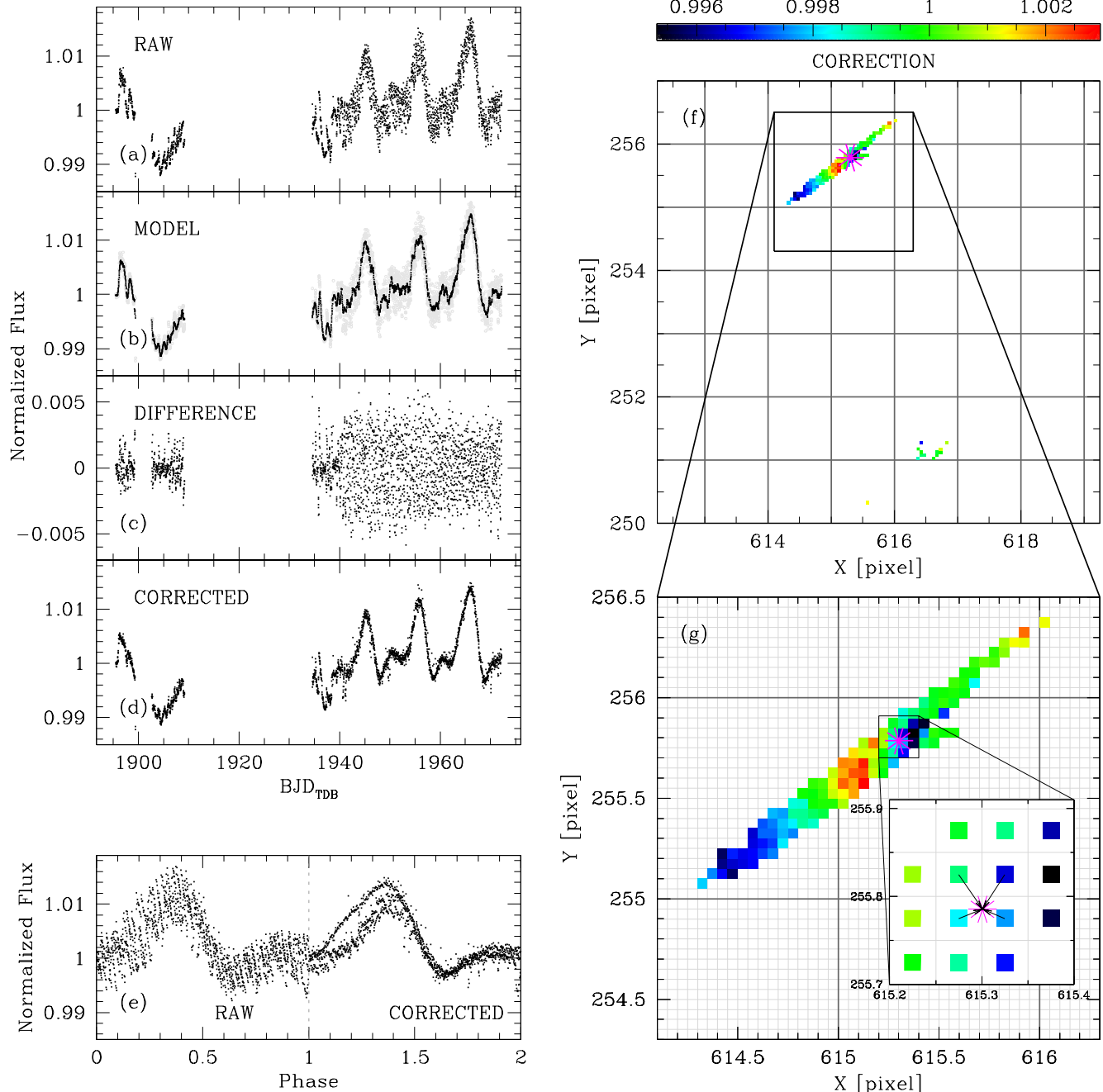


Figure 9. (Left): 3-pixel-aperture LC of star # 1881 (EPIC 209183478) after each step of our correction. From panel (a) to (d): raw LC normalized to its median flux; LC model (black points) put on top of the raw LC (light-gray points); model-subtracted LC; final detrended LC. In panel (e) we show the comparison between the phased (with a period of ~ 10.6 days) LC before (left) and after (right) the correction. It is clear that the drift-induced scatter in the LC is reduced and more details arise, e.g., the LC amplitude of this object changed during the C0. (Right): Outline of our correction. In panel (f) we show the cell and grid-point locations around the star # 1881 loci on the channel 81 over the entire Campaign 0. The thick, dark-gray lines mark the pixel boundaries. The magenta * marks the star location on the channel at a given time. The squares represent the median values of the model-subtracted flux in each of the 0.05×0.05 -pixel-square bins in which each pixel is divided, colour-coded accordingly to the colour bar on top. In panel (g) we zoom-in around the bulk of the points to highlight the sub-pixel elements of the grid (thin, light-gray lines). For the star position at a given time, we used the four surrounding grid points to perform the bi-linear interpolation (sketched with the arrows) and compute the correction.

Fig. 9. For any location on the CCD, the correction was performed by applying a bi-linear interpolation between the surrounding four grid points. The correction was not always available, because for some grid elements there are not enough points to compute the correction. In these cases, no correction was applied.

The whole procedure was iterated three times, each time making an improved LC model by using the LC corrected with the available detrending solution. In Fig. 9 we show the results of the final iteration of our procedure.

Panel (e) of Fig. 9 shows a direct comparison of the folded LC

before (left) and after (right) the correction. The rms is improved and allows us to see more details in the LC.

One advantage of our LC-extraction method is a more robust position measurement. Indeed, as described in Sect. 4, we transformed the position of a target star as given in the AIC into the corresponding image reference system by using a subset of close-by stars, target excluded, to compute the coefficients of the six-parameter linear transformations. The local-transformation approach reduces (on average by a factor N^{-1} , where N is the number of stars used) most of the systematic effects that could harm the stellar positions (e.g., the uncorrected geometric distortion).

The LC detrending is critical both to the removal of the spacecraft-related systematics that degrade the *K2* photometric precision and to pushing *K2* performance as close as possible to that of the original *Kepler* main mission. In Fig. 10 we show the rms (defined as the 3.5σ -clipped 68.27th-percentile of the distribution about the median value of the points in the LC) improvement after the detrending process for the 3-pixel-aperture and PSF photometry on neighbour-subtracted images. The rms was calculated on the normalized LC, i.e. after the LC flux was divided by the 3.5σ -clipped median value of all the flux measurements. As we will see in sub-section 7.2, these two photometric methods are the best-performing methods at the bright- and faint-end regime, respectively. The improvement is greater for bright stars, i.e. stars with high SNR and better-constrained positions; while for faint stars the effect is lost in the random noise.

6.1 A previously unknown 2.04-day periodic artifact

Several LCs turned out to exhibit a periodic drop in their fluxes that we have not seen described anywhere. These drops are rather sharp and resemble boxy transits; we illustrate them in Fig. 11. The period of this effect is ~ 2.04 days, and the drops last for exactly six images, for each of the non-interrupted sub-series within C0. Not all the stars in the affected images show the drop feature.

We extensively investigated the affected and un-affected stars on individual *K2*/C0/channel-81 images and found that the effect could be column-related. The amount of drop in the flux is not always the same and it correlates with magnitude. We have not found any description of such an effect either in the *Kepler* manual or in the literature.

We suspect that it might be due to an over-correction in correspondence of mis-behaving columns. This over-correction might be the result of electronic activities related to the periodic momentum dump of the two remaining reaction wheels through thruster firings; which happens every two days (Howell et al. 2014; Lund et al. 2015). For example, it could be a change in the reading rate.

Another possibility, discussed with the referee, is that this effect can be originated by a non-identical *Kepler*-pipeline processing of contiguous TPFs that can create some un-physical discontinuity. Such 2.04-d periodic effect could only be detected when dealing with more than one TPF at a time, as we did in our reconstructed-image approach.

Lacking more engineering data and detailed knowledge of the on-board pre-reduction pipeline, we have limited ourselves to simply describing and correcting these effects empirically. We first made a model of the LC trend (by applying a running-average filter with a window of ~ 6 hours) and computed the median value of the model-subtracted LC flux for affected and un-affected data points. If the difference between these median values was greater than the model-subtracted LC rms (computed using only the un-affected points), we marked the LC as flux-drop-affected, and cor-

rected it. The correction to add is computed as the difference between the model of the LC with only the un-affected points and the model obtained using only the flux-drop-affected points (see Fig. 11).

The drawback of our correction is obviously that any true variable star with a significant flux drop every 2.04 days was considered as flux-drop affected and corrected accordingly. Of course, since this flux-drop is not periodic across safe-mode sub-series, it is possible to distinguish these events from true eclipses.

6.2 The role of ePSFs in *Kepler*/*K2* images

The ePSF is not only more suitable to performing photometry in crowded regions and for faint stars, but it can also be used as an additional diagnostic tool to discern among exposures that are most affected by some systematic effects, such as the drift motion of the spacecraft. In the following we show that, by taking advantage of all the information that we have from the ePSFs adjusted for each exposure, we can also select the best exposures (that correspond to points in the LCs) to search for variability (Sect 8.1).

In Fig. 12, we show an outline of our best-exposure selection for a variable-candidate LC (AIC star # 9244). It is well known that *K2*/C0 data contain a periodic, systematic effect every ~ 6 hours, related to the thruster-jet firings used to keep the roll-angle in position. Indeed high SNR stars show a well-defined periodic effect every ~ 0.2452 days (and at its harmonics). In the top-left panel of Fig. 12 we show the hand-selected points in the phased LC with a period of ~ 0.2452 days, while in the top-right panel we show the corresponding location of such points during C0. By phasing different LCs with this period, we noticed that there is one group of points (red, solid triangles) that is more scattered than the others. These points are associated with the thruster-jet events. The remaining points, marked with different colours and shapes, represent different portions of the LC. The less populated groups (black, solid squares) were taken during the first part of the campaign; while the more populated clumps (green dots) were taken during the second part of the C0. The remaining outliers (azure, open circles) are those points obtained during the coarse pointing of the spacecraft, flagged in the TPFs accordingly. In practice, we discarded all points corresponding to the first part of C0, and the points collected during the thruster-jet events and coarse pointing.

We found very good agreement between such point selection and the ePSF (middle-left panel) peak and FWHM (middle-right panel). For example, the exposures taken during a thruster-jet event have a less-peaked ePSF because the exposure is blurred during the long-cadence integration time. Hereafter, we use the adjective “*clean*” to define a LC based on the stable part on the second half of the Campaign (green points in Fig. 12). We run our variable star finding algorithms only on the clean LCs.

7 PHOTOMETRIC PRECISION

We used three different parameters to help us to estimate the photometric precision:

- *rms* (defined as in Sect 6);
- *p2p rms*. The point-to-point rms (p2p rms) is defined as the 3.5σ -clipped 68.27th-percentile of the distribution around the median value of the scatter (the difference between two consecutive points);

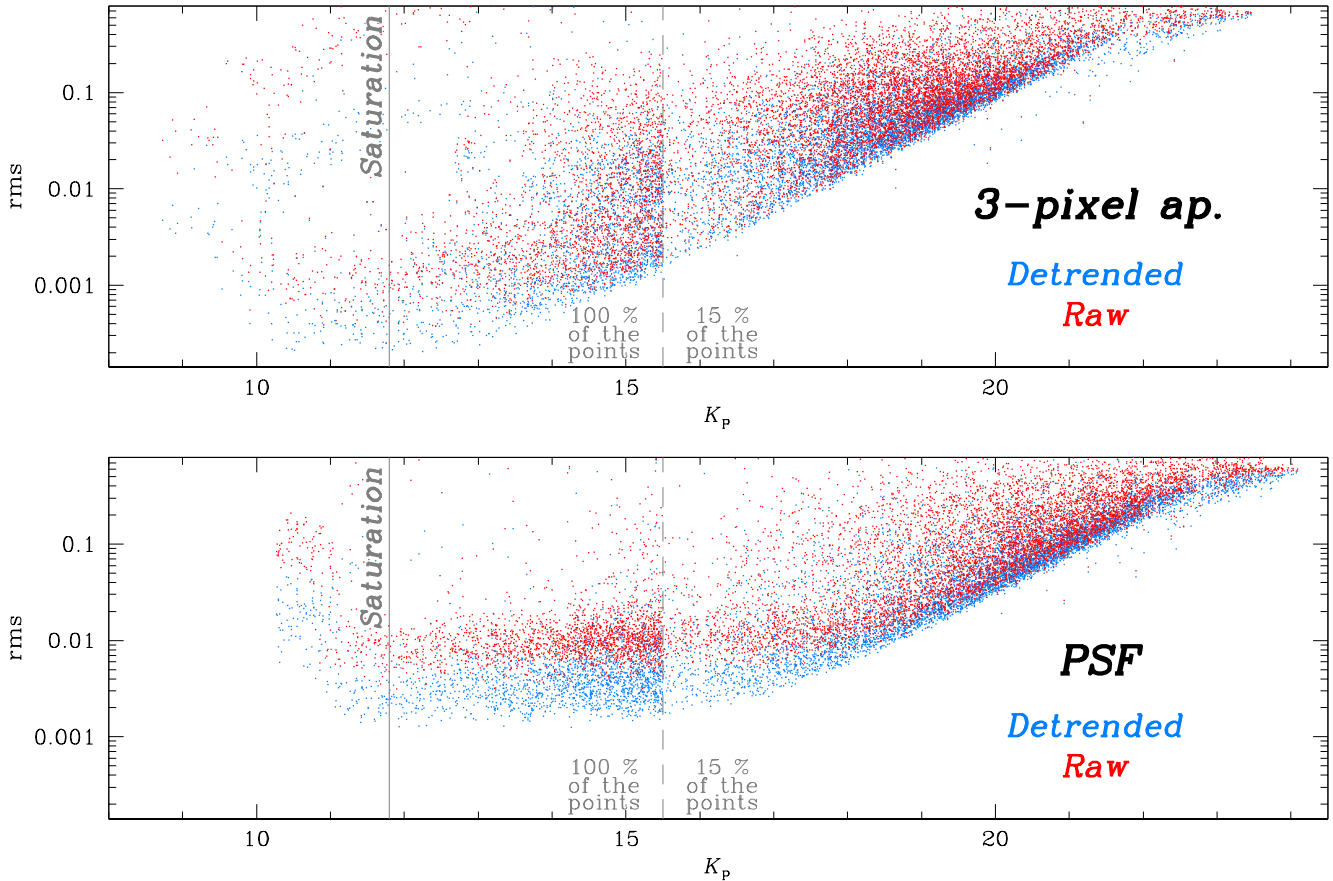


Figure 10. Photometric rms as a function of the K_p magnitude before (red points) and after (blue points) applying our detrending procedure. We plot only the neighbour-subtracted photometry from the two measurements that show the best rms in the bright (3-pixel aperture, *Top panel*) and faint (PSF, *Bottom panel*) regime. For $K_p > 15.5$ (vertical, gray dashed line) we show only 15% of the points for clarity. The vertical, gray solid line is set at the saturation threshold $K_p \sim 11.8$.

- *6.5-hour rms.* The 6.5-hour rms is defined as follows. We processed each available LC with a 6.5-hour running-average filter, and then divided it in 13-point bins. For each bin, we computed the 3.5σ -clipped rms and divided it by $\sqrt{12}$ ($\sqrt{N-1}$, with N the number of points in each bin). The 6.5-hour rms is the median value of these rms measurements.

All three parameters have been calculated on the normalized LC.

Our PSF-based, neighbour-subtracted technique has been specifically developed to deal with crowded regions and faint stars. Therefore, we expect substantial improvements with respect to what is in the literature in these two specific regimes. In the following, we will demonstrate the effectiveness of our new approach.

7.1 Photometry on images with and without neighbours

By subtracting stellar neighbours before measuring the flux of a given star, we can obtain performance comparable with that achieved by others in the literature, but in more crowded regions. In general, within a single 4×4 -arcsec 2 pixel, there can be more than one source that contribute to the total flux. Therefore, we expect the neighbour-subtraction method to be useful not only in stellar clusters or fields in the Galactic bulge, but also in relatively-lower-density regions.

To demonstrate this assertion, we selected two samples of

stars: a “crowded”, sample centered on NGC 2158, and an “isolated” sample, that comes from five different regions where the stellar density is lower. The two samples contain the same number of sources. We computed the LC rms for a 3-pixel aperture and for PSF photometry with and without subtracting stellar neighbours (Fig. 13).

Without removing stellar neighbours, the light of close-by stars that falls within the aperture increases the target flux, alters the faint-end tail of the rms trend (naturally, the problems becomes larger for larger apertures). The effect is more evident in crowded regions, in particular when using aperture photometry. For the 3-pixel aperture photometry, in the crowded region the limiting magnitude on the original images is $K_p \sim 18$, to be compared with the $K_p \sim 22$ limiting magnitude in neighbour-subtracted images of the same field (second-to-the-last panels in Fig. 13). In summary, in crowded regions, by using the neighbour-subtracted images, we obtained a more reliable stellar flux and gained about 4 K_p magnitudes for the 3-pixel-aperture photometry. Furthermore, for both aperture and PSF photometry, we have a lower rms for the LCs, and the bulk of the LC-rms distribution as a function of magnitude looks sharper. In conclusion, hereafter we will consider only neighbour-subtracted LCs.

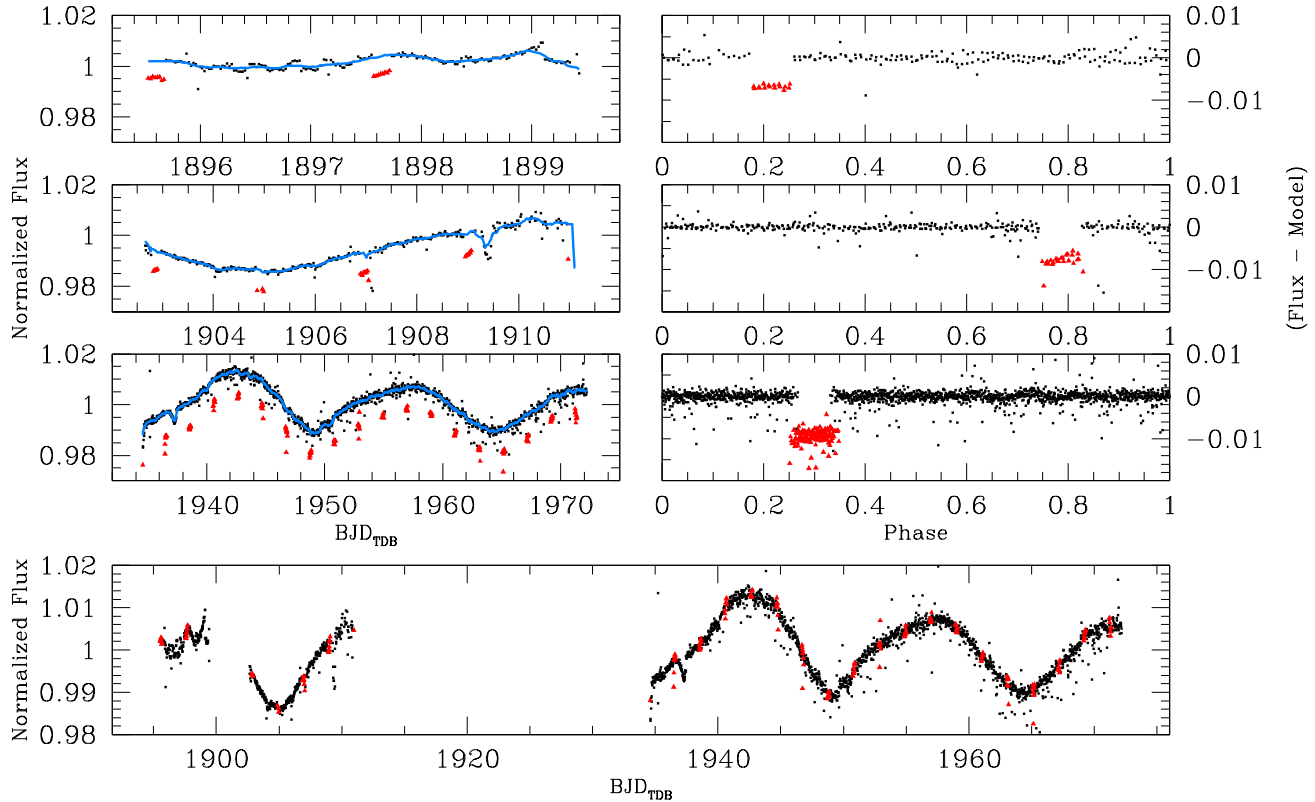


Figure 11. Example of a LC (AIC # 8600, 5-pixel-aperture photometry) affected by the flux-drop effect described in Sect. 6.1. From *Top*, in the first-row panels we show the first sub-series (before the first safe mode) of points of the C0/channel-81 LC (*Left*) and the corresponding phased LC with a period of 2.04 days (*Right*). In the second and third rows we show the same as above but for the second (between the first and the second safe modes) and third (after the second safe mode) sub-series of the LC and the phased LC. The black dots represent the unaffected points, the red triangles are the photometric points affected by the flux drop. The azure line is the LC model. Note that the phase at which the flux drop occurs is not the same in the different parts of the LC, meaning that this effect could be related to the instrumentation, and that it is reset after each break in the C0. Finally, in the *Bottom* panel we plot the corrected LC.

7.2 Photometry on bright and faint stars

As expected, and as shown by Nardiello et al. (2015) for ground-based data, aperture photometry performs, on average, better on isolated, bright stars, while the PSF photometry gives better results on faint stars. In Table 1 and 2 we list the rms values in part-per-million (ppm) for each of the five photometric methods we adopted.

As can be inferred from these Tables, for bright stars, 3-pixel-aperture photometry shows, on average, lower rms than 5- and 10-pixel aperture photometry. The 1-pixel-aperture- and the PSF-based photometry have almost the same trend in the faint star regime ($K_p \geq 15.5$), with the 1-pixel aperture showing a slightly smaller rms for $K_p > 19$, while the PSF photometry performs 2-3 times better on brighter stars. In the following discussion, for faint stars, we prefer to use PSF rather than 1-pixel-aperture neighbour-subtracted photometry, although, on average, equivalent in terms of photometric scatter.

In Fig. 14 we show a comparison between the PSF and the 3-pixel aperture photometric methods. It is clear that for $K_p > 15.5$ the PSF photometry performs better than the 3-pixel aperture.

For bright stars, the 3-pixel-aperture 6.5-hour rms is below 100 ppm between $10 < K_p < 14$, with a best value of about 30 ppm for stars with $11 < K_p < 12.5$. For stars brighter than $K_p \sim 10$, the rms increases, mainly because we are working on heavily-saturated stars. In the faint-end regime, using PSF photometry we obtained 6.5-hour rms 2-3 times better than using a 3-pixel-aperture photometry.

At $18 < K_p < 19$ the 6.5-hour rms is about 2600 ppm. Such precision allows us to detect a flux drop of a few hundredths of magnitude, i.e., the LC dimming due to exoplanet candidate TR1 discovered by Mochejska et al. (2006). We will further discuss this object in Sect. 9.

In conclusion, we find that even at the bright end our neighbour-subtracted technique allows us to obtain performance that is comparable to those in the literature. This is the case even though we are dealing with a more crowded region than most previous studies.

7.3 Comparison with existing works on *K2* data

At present, there are a number of studies in literature that are focused on the Campaign 0 data of *K2*. Here, we provide a comparison, both using the LC rms and through a visual inspection of the LCs, for the objects in common with previous published studies.

Before making such a comparison, we warn the reader about some aspects that should be taken into account in the following. A fair comparison should be made by comparing the single light curves point by point. Unfortunately, thus far, no one has ever attempted to measure all stars in the entire super-stamps. Rather it is more common practice to restrict the analysis to the outer parts of dense stamps, where the crowding is less severe.

That said, we do have several LCs from stars in common with

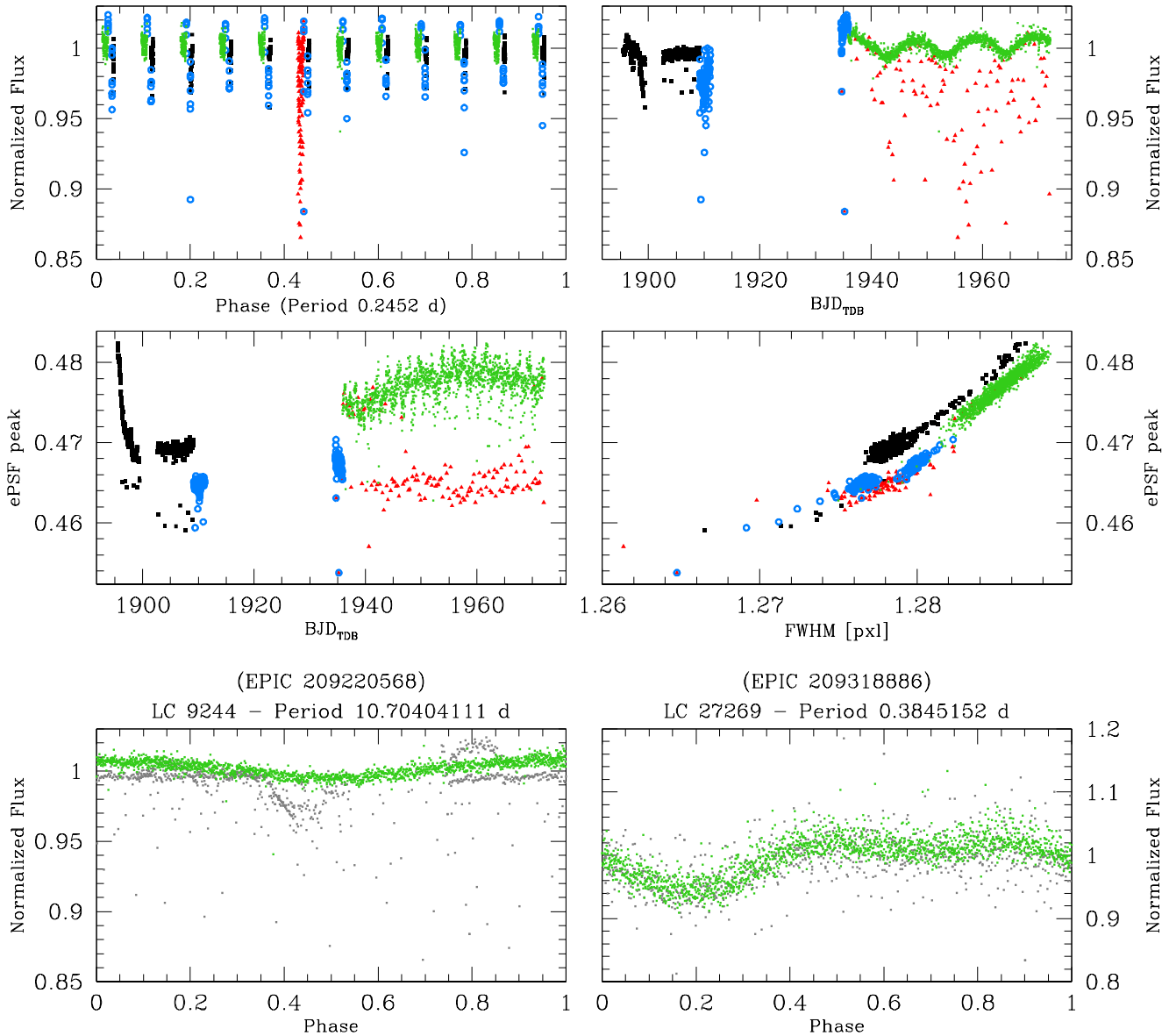


Figure 12. Clean LC definition. In the *Top-left* panel, we show the phased LC with a period of 0.2452 days for the object # 9244 in the AIC. We mark with black filled squares the points obtained before the second safe mode during the C0 observations and with azure, open circles the points corresponding to the “coarse pointing” flag in the original TPFs. The red triangles highlight the exposures that are associated to a thruster-jet event. Finally, with green dots we show the best 1629 out of 2422 points (exposures) for the LC analysis. In the *Top-right* we show the normalized flux as a function of the time for the same LC, with the points colour-coded as before. In the *Middle-left* panel we plot the peak value of the perturbed ePSF of each exposure as a function of time. In the ePSF peak-FWHM plane (*Middle-right* panel) it is also clear that there is a correlation between every effect that could harm the observations and the ePSF. This is an hint of the usefulness of the ePSF parameters as a diagnostic tool. Finally, in the *Bottom* panels we show the LC for the bright object illustrated above (*Left*) and for a fainter star (*Right*, AIC # 27269) in which we plot with green and gray dots the good and the bad points, respectively.

various studies; in the best case (Vanderburg & Johnson 2014), we have 40 stars. Furthermore, by simply comparing the rms given in the different papers, we could introduce some biases. For example, the rms in a given magnitude bin can be overestimated by the number of variable stars within that bin; the methods adopted to compute the rms can be different; there might be different calibration methods to transform “raw” magnitudes into the *Kepler* photometric system. In the latter case, stars can fall in different magnitude bins in different papers. Finally, our neighbour-subtracted LCs are less affected by neighbour-light contamination. As noticed above, the light pollution would result in a brighter LC, which would move

the star into a brighter magnitude bin, and decrease its rms (because of the higher number of counted photons).

7.3.1 Comparison with Vanderburg & Johnson (2014)

The first published study on *K2* photometry was that of Vanderburg & Johnson (2014), and was based on the Engineering data set. The Campaign 0 data set was subsequently reanalyzed by Vanderburg (2014), who worked to improve the photometric performance for fainter stars.

We downloaded from the MAST archive all his LCs for the

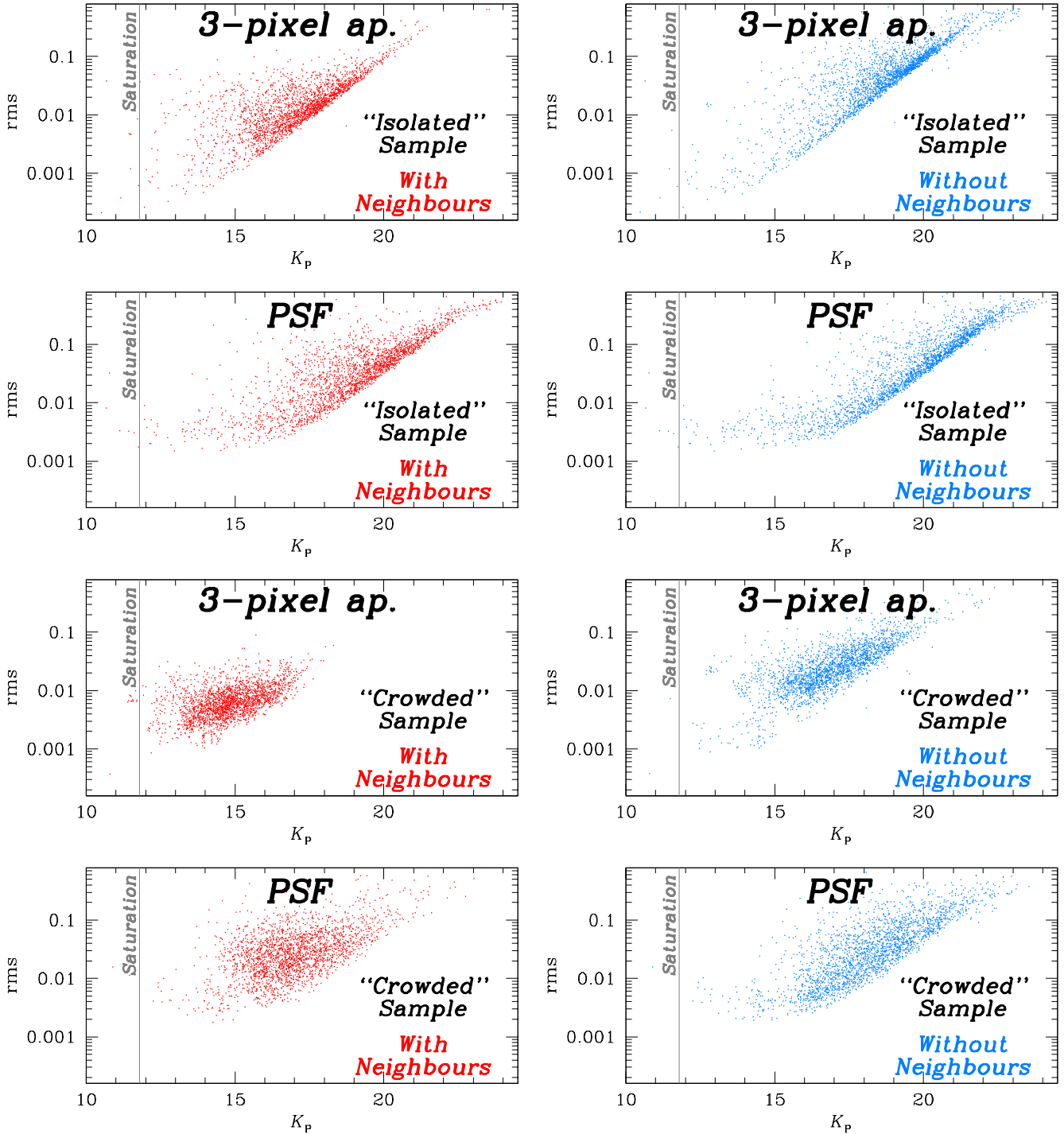


Figure 13. Photometric rms of LCs extracted from the original (red points in *Left* panels), and the neighbour-subtracted (blue points in *Right* panels) images as a function of the K_p magnitude. We show the rms trend for the “isolated” (the first and second rows from *Top*) and the “crowded” (the third and fourth rows) samples, defined as described in the text, for LCs obtained using a 3-pixel aperture and the PSF. The saturation threshold is set at $K_p \sim 11.8$ (vertical, gray solid line).

targets within channel 81, and found 40 objects in common with our catalogue. We computed the three rms as described above. The LCs from Vanderburg (2014) show, on average, a larger p2p and 6.5-hour rms than our LCs for the variable objects, but their p2p and 6.5-hour rms for non-variable stars was lower. While the former behavior was predictable, (as reported by Vanderburg & Johnson

2014, their self-calibrated-flat-field approach works best on dwarfs rather than on highly-variable stars) the latter trend was unexpected. Therefore, we also visually inspected the location of all

Table 1. Photometric precision of the 3-pixel-aperture- and PSF-based photometry evaluated as described in Sect. 7. The values are given in part-per-million. We used the clean LCs to compute these quantities. When no stars were found in a given magnitude interval, we inserted a “/” in the corresponding cell.

K_p Magnitude interval	3-pixel aperture			PSF		
	rms	p2p	6.5-h rms	rms	p2p	6.5-h rms
8 - 9	4365	1994	840	/	/	/
9 - 10	4550	1915	771	/	/	/
10 - 11	3083	433	101	18231	3918	2054
11 - 12	446	124	44	2636	949	424
12 - 13	744	168	62	3300	1068	459
13 - 14	926	276	97	3200	983	439
14 - 15	1977	585	196	3871	1085	489
15 - 16	5720	1882	633	3988	1274	528
16 - 17	10631	4731	1606	4822	1875	693
17 - 18	21219	9533	3176	7214	3518	1189
18 - 19	40885	19749	6564	14070	7936	2601
19 - 20	76625	41163	13534	32813	18376	6150
20 - 21	159131	89546	29876	71199	40570	13456
21 - 22	327174	179254	71173	153875	89963	30335
22 - 23	487721	282520	109300	309403	179357	73297
23 - 24	606784	412491	140349	468002	292661	114074

Table 2. As in Table 1, but for 1-, 5- and 10-pixel-aperture-based photometry.

K_p Magnitude interval	1-pixel aperture			5-pixel aperture			10-pixel aperture		
	rms	p2p	6.5-h rms	rms	p2p	6.5-h rms	rms	p2p	6.5-h rms
7 - 8	/	/	/	/	/	/	5222	2032	917
8 - 9	/	/	/	3983	1758	802	3640	1230	582
9 - 10	/	/	/	8641	2982	1558	6083	2311	1152
10 - 11	9126	5411	1755	10449	4554	1745	18628	7103	3199
11 - 12	5625	3552	1122	451	116	43	1397	261	87
12 - 13	5594	3461	1098	1023	246	87	2972	1081	437
13 - 14	5589	3482	1113	3959	989	387	10915	3876	1350
14 - 15	5918	3484	1115	7777	2897	1043	15341	6028	2083
15 - 16	6108	3566	1141	13369	5306	1866	24145	10945	3738
16 - 17	6473	3743	1201	21162	8917	3056	44430	21238	7173
17 - 18	8003	4477	1439	39276	17885	6022	84555	43223	14664
18 - 19	13766	7833	2521	69978	36431	12105	170644	91746	34174
19 - 20	30515	17248	5557	141595	77484	26331	285471	134808	69279
20 - 21	66356	37814	12241	299378	158724	63791	404477	185638	87072
21 - 22	141837	83477	27306	432749	225126	97786	528062	289481	116628
22 - 23	301746	173745	66720	591510	359285	128364	587527	373223	138088
23 - 24	447170	287843	106035	687907	511448	147173	/	/	/

stars in common on the images and the regions covered by the adopted aperture masks⁸.

For bright stars, Vanderburg (2014) used a circular aperture that included several neighbour sources. For faint stars, the ad-hoc aperture that was designed to avoid light contamination works only partially, since the flux on the wings of the PSF can still fall inside it. Furthermore, for blended stars the adopted aperture mask included all of them and, finally, the EPIC catalog seems not complete enough. In either cases, the total flux of the source is increased because of the contribution of the neighbours, resulting in a higher SNR for the source (with a consequent better Poisson rms), but this does not correspond to the true SNR of the individual target source. Of course, we cannot exclude that Vanderburg (2014) detrending algorithm works better, further improving the final rms. A larger sample of stars is required for a more conclusive comparison.

⁸ <https://www.cfa.harvard.edu/~avanderb/k2.html>

We also found that at least two variable objects identified by Vanderburg (2014) were mismatched/blended, difficult for him to identify due to the limitations introduced by the EPIC (bright, isolated objects) and to the low resolution of the *K2* images (see next Section).

It is worth to mention that Vanderburg (2014) releases for each light curve a flag that marks the cadence number associated to a thruster-jet event. We compared their flag with our flag described in Sect. 6.2. Among the cadences in common between the two works, we found that we flagged (and do not use) a lower number of images. This is probably due to our perturbed-PSF approach that is able to fit reasonably well objects imaged while the thruster-jet effect was not severe. However, we found a good agreement between the two thruster-jet-identification methods.

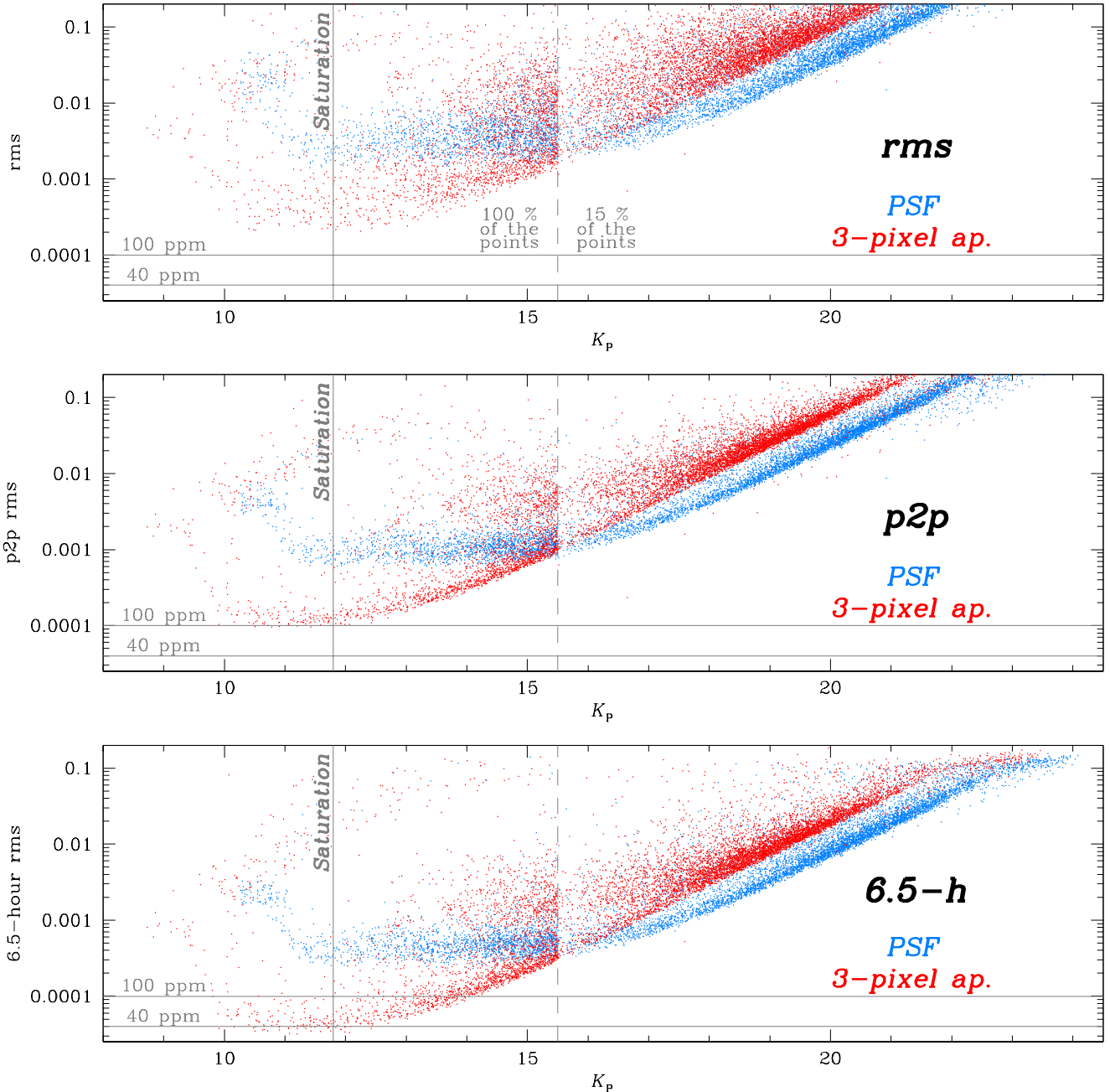


Figure 14. Photometric rms (*Top*), p2p rms (*Middle*) and 6.5-hour rms (*Bottom*) as a function of the K_p magnitude derived from the 3-pixel-aperture- (red points) and PSF-based (blue points) neighbour-subtracted LCs. The vertical, gray dashed line is set at $K_p=15.5$. For stars fainter than $K_p\sim 15.5$ the PSF photometry has a lower rms. The vertical, gray solid line is set at the saturation threshold ($K_p\sim 11.8$). As a reference, we plot two horizontal, gray solid lines at 100 and 40 parts-per-million (ppm), respectively. As in Fig. 12, for $K_p>15.5$ we show only the 15% of the points, for clarity.

7.3.2 Comparison with Armstrong *et al.* (2015)

Armstrong et al. (2015) released C0 LCs obtained with a similar method and with comparable performance to those of Vanderburg & Johnson (2014). We downloaded the LCs from their archive⁹ and computed the rms for the 12 objects we have in common. Again, we found that our photometry provides LCs with a lower rms for almost all these variable stars.

As the rms cannot give a direct measurement of the goodness of the photometry, we made a visual comparison of the 12 LCs in common between our data set and Armstrong et al. (2015) one. In Fig. 15 we show the LC comparison of 10 out of 12 objects in common. We also included the LCs of Vanderburg & Johnson (2014) since these objects are present in their sample too. We plotted the best photometry for all the LCs. On average, our LCs looks sharper (e.g., LC 4710).

Fig. 16 shows the first of the remaining two objects we have in common. EPIC 202073445 is an eclipsing binary. The

⁹ <http://deneb.astro.warwick.ac.uk/phrlbj/k2varcat/>

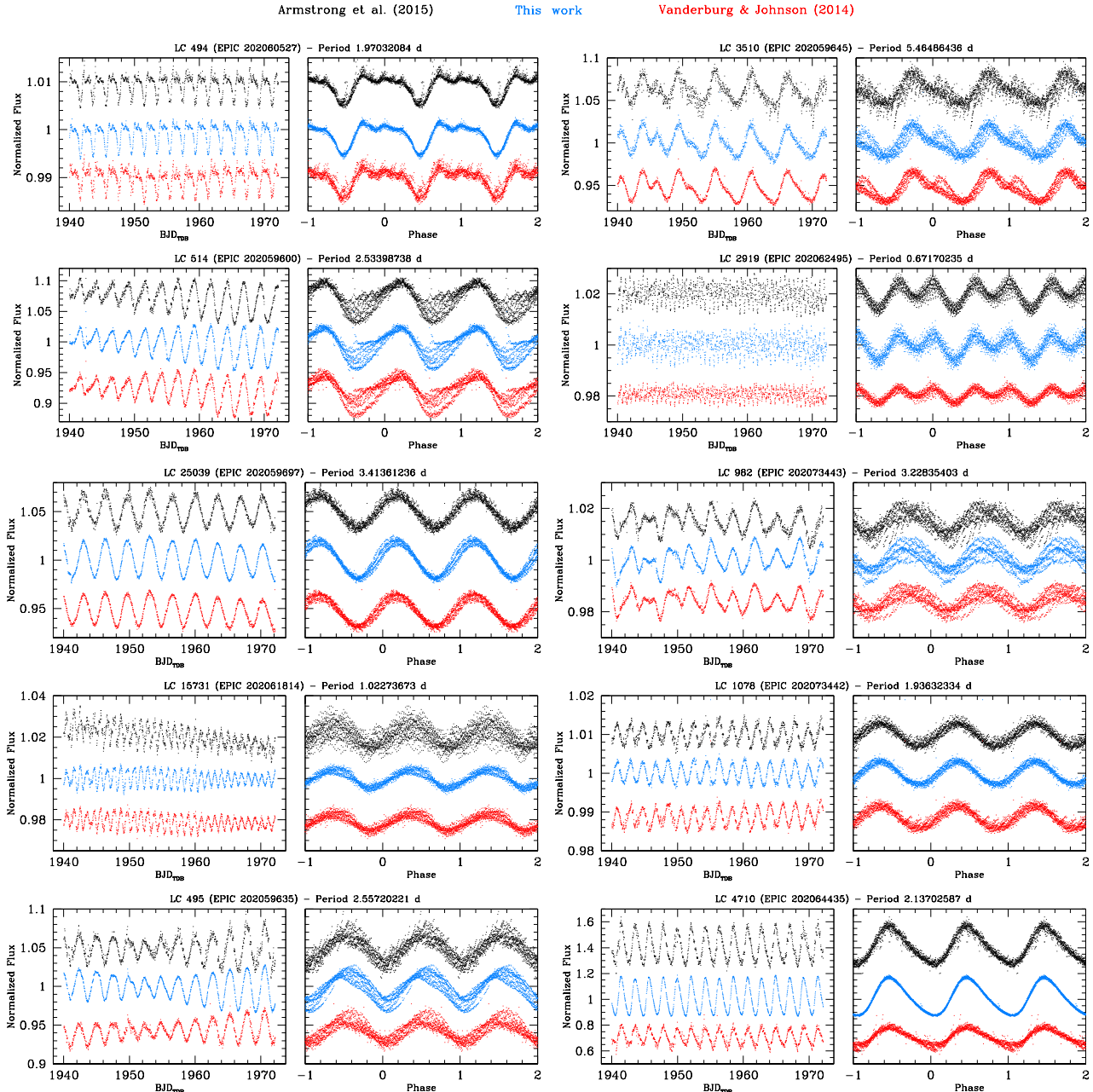


Figure 15. Point-by-point comparison between our light curves (azule points) and those from Vanderburg & Johnson (2014) (red) and Armstrong et al. (2015) (black). We show only the points imaged at the same BJD_{TDB} in common among the three works.

depth of our LC is smaller than in the other two papers. However, Nardiello et al. (2015) found that the real eclipsing binary is another star (namely, EPIC 209186077), very close to EPIC 202073445. To further shed light on this ambiguity, we compared the LCs of both stars using different kinds of photometry. The mismatched eclipsing binary does not show any flux variation with the PSF and 1-pixel-aperture photometry. On the other hand, the larger the aperture, the deeper the eclipse. Instead, the “real” eclipsing binary shows that the eclipses become dimmer and dimmer with increasing aperture radius, as expected since its flux is diluted by the remaining flux of the (un-)subtracted neighbours. We confirm that the true eclipsing binary is the one identified by Nardiello et al. (2015) (EPIC 209186077). This mis-identification

is also present in the eclipsing-binary catalogue of LaCourse et al. (2015).

There is a similar ambiguity between EPIC 202059586 and EPIC 209190225 (Fig. 17). Again, comparing the PSF- and aperture-based LCs, we found that the first object is rather an aperiodic star that shows a flux modulation due to the latter object, while the second one is the real variable.

7.3.3 Comparison with Aigrain et al. (2015)

Aigrain et al. (2015) developed a different method, which is described in detail in their paper. Their approach has some similar-

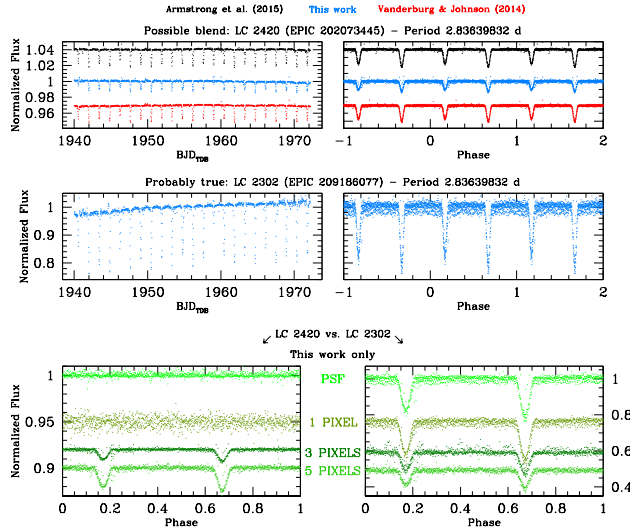


Figure 16. LC comparison between EPIC 202073445 (LC # 2420 in AIC) and EPIC 209186077 (LC # 2302). On the *Top* panels we compared our LC of the probable-blend object (EPIC 202073445) with those found in the literature as in Fig. 15. In the *Middle* panels we show the LC of the object that we found to be the true variable (EPIC 209186077). We show only our LC since these objects are neither in Vanderburg & Johnson (2014) nor in Armstrong et al. (2015) data set. In the *Bottom* panels we finally show our LCs colour-coded with different shades of green according to the photometric method (PSF, 1-, 3- and 5-pixel aperture).

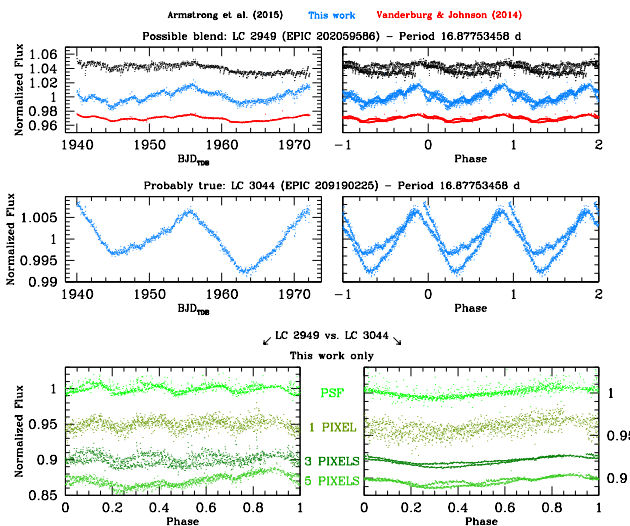


Figure 17. As in Fig. 16, but for the case of EPIC 202059586 (LC # 2949) and EPIC 209190225 (LC # 3044).

ties with the effort here described, e.g., the image reconstruction and the adoption of an input list. Unfortunately, a proper comparison is not possible since they analyzed only the Engineering data. Campaign 0 showed different problems and lasted longer. Anyway, for the sake of completeness, we compared their results with our LCs.

Due to its less-ambiguous definition, we compared the p2p rms. In the brightest magnitude intervals ($9 < K_p < 11$), Aigrain et al. (2015) shows a better p2p rms than we derived here. In the interval $11 < K_p < 15$, our 3-pixel-aperture p2p rms ranges from 124 to 585 ppm; while their p2p rms varies between 238 and 867 ppm. For

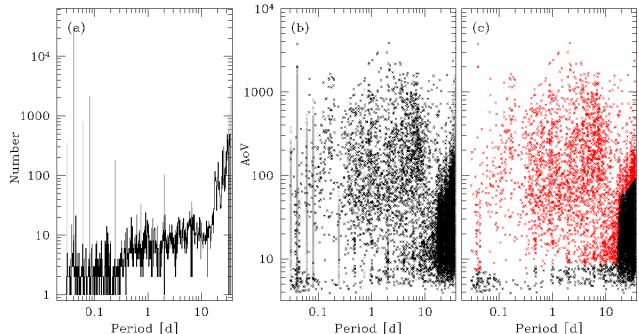


Figure 18. Example of candidate-variable selection using the AoV algorithm. Panel (a): the distribution of the periods; in black we show the distribution after removing the spikes, in grey the removed spikes. Panel (b): LC periods as a function of the AoV metric Θ for all the stars; the stars that have passed the first selection are plotted in black, the stars having periods corresponding to the removed spikes in gray. Panel (c): periods of light curves as a function of Θ after spikes suppression. Red dots represent variable candidates.

fainter magnitudes up to $K_p \sim 19$ our p2p rms is slightly better. On the other hand, our PSF-based photometry performs much better in the magnitude interval $15 < K_p < 19$, with a minimum p2p-rms value of 1274 ppm and a maximum of 7936 ppm, to be compared with that of Aigrain et al. (2015) that increases from 1841 to 23673 ppm in the same magnitude range. It is worth to mention that we could measure objects up to 5 magnitudes fainter than those measured by Aigrain et al. (2015).

8 VARIABLE CANDIDATES

8.1 Search for Variables

In order to detect candidate variable stars, we followed the procedure adopted by Nardiello et al. (2015); we describe the basics of the procedure below. We obtained the periodograms of all clean LCs using three different tools included in the VARTOOLS v1.32 package, written by Hartman et al. (2008) and public available¹⁰:

- The first tool is the Generalized Lomb-Scargle (GLS) periodogram (Press et al. 1992; Zechmeister & Kürster 2009), useful in detecting sinusoidal periodic signals. It provides the formal false alarm probability (FAP) that we used to select variable-star candidates.
- The second tool is the Analysis of Variance (AoV) periodogram (Schwarzenberg-Czerny 1989), suitable for all kind of variables. We used the associated AoV FAP metric (Θ) that is a good diagnostic useful to select stars that have a high probability to be variables.
- The third tool is the Box-fitting Least-Squares (BLS) periodogram (Kovács, Zucker, & Mazeh 2002), particularly effective when searching for box-like dips in an otherwise-flat or nearly-flat light curve, such as those typical of detached eclipsing binaries and planetary transits. We used the diagnostic “signal-to-pink noise” (Pont, Zucker, & Queloz 2006), as defined by Hartman et al. (2009), to select eclipsing-binary and planetary-transit candidates.

Figure 18 illustrates the procedure used to identify candidate variables resulting by the application of the AoV finding algorithm.

¹⁰ <http://www.astro.princeton.edu/~jhartman/vartools.html>

The same procedure has been adopted for the GLS and BLS finding algorithms. First, we built the histogram of the periods (P) of all clean LCs, as shown in panel (a) of Fig. 18. For each period P_0 we computed the median of the histogram values in the bins within an interval centered at P_0 and extended by $50 \times \delta P$, where δP is the bin width chosen to build the histogram. We flagged as “spike” the P_0 corresponding to a histogram value 5σ above that median, where σ is the 68.27th percentile of the sorted residuals from the median value itself. These spikes are associated with spurious signals due to systematic effects such as, e.g., the jet-firing every ~ 5.88 hours, the long cadence at ~ 29 minutes (~ 0.02 d) and the periodicity of ~ 2.04 days (described in Sect. 6.1) and their harmonics. Finally, we removed from the catalogue the stars having periods inside $P_0 \pm \delta P/2$, keeping only those with high Θ . We performed our searching to periods between 0.025 (slightly higher than the long-cadence sampling) and 36.5 d (clean-LC total time interval). GLS, AOV and BLS input parameters were chosen to optimize the variable finding and are not perfect. Indeed, we selected a sample of known variables and tuned the input parameters in order to maximize the signal-to-noise ratio outputted by each of the three findings. This way, some variables could have been missed because the three tasks found the highest SNR with a wrong period, e.g., the 0.04-d alias.

In panel (b) of Fig. 18, for all clean LCs, we plot the Θ parameter as a function of the detected period, highlighting the objects removed because their period coincides with a spike. In panel (c) we selected by hand the stars that have high Θ .

We ran the VARTOOLS algorithms GLS, AoV, and BLS on a list of 52 596 light curves. We initially excluded all objects that in our input list were outside the *K2* TPFs. Then, for each star, we selected the photometry (1-, 3-, 5-, 10-pixel aperture or PSF) that gives the best precision at a given magnitude, according to what was described in Section 7, Fig. 14, and Tables 1 and 2.

We combined the lists of candidate variables obtained by applying the three variable-detection algorithms and visually inspected each of them. We excluded all obvious blends by looking at the LC-shape and position of each star and of its neighbours within a radius of about 11 *K2* pixels (~ 43 arcsec).

We found a total of 2759 variables of which 1887 passed our visual inspection as candidates and 202 were flagged as blends. The remaining 670 LCs were difficult to visually judge. We included them into our final catalogue, but added a warning flag indicating that their variable nature is in doubt.

8.2 Comparison with the literature and sample improvement

In order to evaluate the completeness of our sample, we matched the AIC with six catalogues found in the literature: Hu et al. (2005), Jeon & Lee (2010), Kim et al. (2004), Meibom, Mathieu, & Stassun (2009), Mochejska et al. (2004, 2006) and Nardiello et al. (2015). These studies, which all cover the M 35/NGC 2158 super-stamp region, analyzed different aspects of stellar variability and made use of different observational instruments and detection techniques (e.g., Meibom, Mathieu, & Stassun 2009).

Cross-correlation of these catalogue results in 658 common entries. Of these, 555 sources are also present in our AIC. The remaining 103 objects are missing for various reasons. A small fraction ($\sim 10\%$) of stars had a very-bright neighbour source that was badly subtracted because the PSF is still far from perfect or were just too close to the edge of our field of view. For the remaining missing known variables, we found that the periods given by the three VARTOOLS algorithms were close to that of a spurious signal

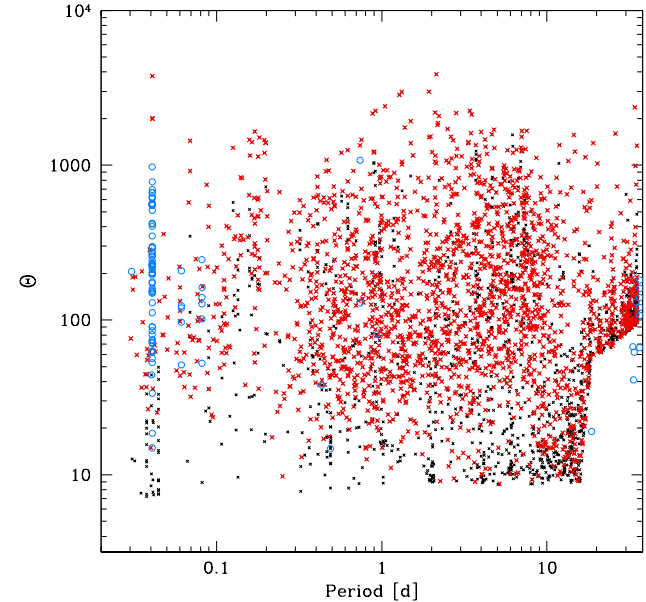


Figure 19. Periods of the light curves as a function of Θ for all the candidate variables. With red crosses we show all variables we found in our analysis of the *K2* data, with azure, open circles the variable stars from published catalogues and present in our AIC we failed to identify among our *K2* LCs. All these variables are included in our final catalogue of variable candidates, with different flags. Black crosses represent all variable sources that passes our first selection described in Fig. 18 but not our visual inspection (see text for detail).

(spikes in the AoV vs. period plot of Fig. 18) or lied below our selection threshold (panel c in Fig. 18). Therefore they were excluded before the visual check, even if their LCs showed a clear variable signature. As an example, we show in Fig. 19 the AoV parameter Θ as a function of LC period for all the candidate variables¹¹ in which we marked with a different colour the location of such missed objects. Since there is no reason to exclude them, we added such previously-discovered variables to our catalogue.

The variable stars found in the literature were also useful to refine our sample and remove some blends and fake detection left after the visual inspection of the LCs. Indeed, previous published studies have made use of images with a higher resolution than that of *K2*, and therefore we chose to rely on the former in ambiguous cases.

After this second refinement of our catalogue, we have 2133 candidate variables, 444 sources with possible blends or dominated by systematic effects, and 272 objects for which the LC is difficult to interpret. In the final catalogue that we release with this paper, we will properly flag all these different sources (see Sect. 10). In any case, we will release all LCs extracted from the *K2*/C0/channel-81 data, which will be available to anyone for any further investigation. In Appendix A we show 10 LCs as example.

¹¹ Irregular and long-period objects, such as the cataclysmic variable V57 found by Mochejska et al. (2004) (period ~ 48 days) for which we can see only one peak in the clean LC, are plotted with an arbitrary period ~ 36.5 days.

8.3 Variable location on the M35 and NGC 2158 colour-magnitude diagrams

We also used the $BVRJ_{2\text{MASS}}H_{2\text{MASS}}K_{2\text{MASS}}$ and white-light-magnitude catalogue of Nardiello et al. (2015) to find the location of our variables in the colour-magnitude diagrams (CMDs). In Fig. 20, we show the B vs. $(B - R)$ CMDs of the star sample used to search for variable candidates (Sect. 8.1) that have a B - and R -magnitude entry in the catalogue. We plot candidate variables, difficult-interpretation objects and blends in different boxes in order to better illustrate the three samples (panels a, b and c).

9 TR1 AS A PROCEDURE BENCHMARK

Mochejska et al. (2004, 2006) made an extensive ground-based campaign search for transiting exoplanets in NGC 2158 and, among the discovered variable sources, they found an exoplanet candidate with a transit depth of ~ 0.037 magnitudes (TR1, following their nomenclature). Mochejska et al. (2006) suggested that TR1 could be a hot-Jupiter with a period of 2.3629 days. The hosting star is a NGC 2158 member, $V_{\text{max}} \simeq 19.218$, $R_{\text{max}} \simeq 18.544$, $(\alpha, \delta)_{\text{J2000.0}} \sim (06^{\text{h}}07^{\text{m}}35\text{s}4, +24^{\circ}05'40''8)$.

This object represents an ideal test-bed for our independent pipeline reduction of *Kepler*/K2 data in crowded regions. Figure 21 shows the region of sky around TR1 in images collected with three different instruments and completely different resolutions. The light pollution of target neighbours is evident. In the left panel, we show an $\sim 10 \times 10$ arcmin 2 region (North up and East left) around TR1 from the *K2* stacked image of channel 81. A green circle of radius 3 *Kepler* pixels and a red square of 1 *Kepler* pixel per side centered on TR1 are barely visible in this panel. In the middle-left panel, a zoomed-in image of about 25×28 arcsec 2 centered on TR1. The yellow grid represents the *Kepler* CCD pixels. The red square shows the location of TR1. It is clear that, without knowing the positions of the target, TR1 identification would be hard if not impossible. The middle-right panel shows the same region, but from the Schmidt filter-less stacked image of Nardiello et al. (2015). In this image the pixel scale is ~ 0.862 arcsec pixel $^{-1}$. The higher spatial resolution of this instrument allows us to better identify TR1. We can identify at least 11 TR1 neighbours within the 3-*Kepler*-pixel aperture. These stars badly pollute the target LC, dimming the transit, and therefore leading to an underestimated radius if we do not properly account for their contribution. Finally, in the right-most panel, we show the same region as seen in an ACS/WFC@*HST* F606W-filter stacked image described in Bedin et al. (2010) (from GO-10500, PI: Bedin). In this case, the pixel scale is about 25 mas pixel $^{-1}$ and the image shows that, within a single *Kepler* pixel, there can be more than one star. Figure 22 shows an individual *K2* exposure before and after subtraction of neighbour sources present in the input list.

The *Kepler* magnitude of TR1 is $K_{\text{p,max}} \simeq 18.35$. Therefore, this object is at the faint end of most of the previous studies. With the photometric technique developed in this paper, TR1 becomes a well-measurable object, as we can push our photometry almost 5 magnitudes fainter and measure stars in crowded environments. In this magnitude interval and at this level of crowding the 1-pixel-aperture and the PSF-based photometry are the only two photometric approaches that allow us to measure the light dimming in TR1 LC.

Despite the *Kepler* pixel size, and consequent neighbour contamination, the detrended light curve from *K2* data is significantly

more complete and precise than that of Mochejska et al. (2006). Figure 23 shows the phased and detrended clean LCs. In the top panel, we plot the original, detrended LC. In the other panels we show the same LC after we applied a running-average filter of 24-h window to remove any systematic trend and/or long-period LC variability in order to better highlight TR1 transits. The period we found using the BLS algorithm is of 2.36489338 days. In Fig. 23 we phased the light curve with double the period.

In the phased LC, both eclipses have more a “V”-like than a “U”-like shape¹². If we also consider the location of TR1 in the CMD (*Right* panel of Fig. 23), it appears more likely to be a binary with a grazing eclipse rather than a transiting exoplanet candidate. In a future paper of this series we will make use of the input list from *HST* data to better characterize TR1. We will also better determine the LCs for the subsample of stars that fall within the ACS/WFC footprint of the *HST* program GO-10500 field.

An important by-product of our method is that we can much-better measure the depth of the eclipses, since our transits are less diluted by the light coming from neighbour sources than other approaches. Figure 24 shows a comparison between the detrended clean TR1 LCs with (black points) and without (azure points) TR1 neighbours. The uppermost LCs were those obtained with 3-pixel-aperture photometry, while those in the middle and in the bottom were extracted using the PSF photometry. We phased these light curves with a period of ~ 4.73 d as in Fig. 23. In the right panel we also binned the LCs with bins of 0.01 phase each and computed, within such each bin, the median and the 68.27th percentile of the distribution around the median values.

The 3-pixel-aperture-based LCs do not show any significant flux variation. The median magnitude is three magnitudes brighter and the rms is smaller than in the PSF-based LCs; all evidences of neighbour-light contamination as discussed in Sect. 7. This LC represents the result of a classic approach found in the literature.

On the other hand, the remaining PSF-based LCs with (hereafter wLC) and without (w/oLC) neighbours clearly present at least one flux drop. First of all, TR1 in the wLC is about 0.25 magnitudes brighter than in the w/oLC. The w/oLC does not only show a smaller rms and fewer outliers, but it shows two distinct eclipses; while the wLC exhibits only the eclipse around phase ~ 0.2 .

Using VARTOOLS BLS and EXOFAST suit (Eastman, Gaudi, & Agol 2013, assuming TR1 is a transiting exoplanet), we estimated a TR1 eclipse depth on the w/oLC (assuming the original BLS period of ~ 2.36 days) of about 3.2% and 3.4%, respectively. Taking into account (1) that our LC and that of Mochejska et al. (2006) are obtained from different pass-bands, (2) the measurement errors, (3) the *K2* integration time lasts half an hour, and (4) the incompleteness of the AIC, we conclude that the two values are in rather good agreement. Therefore, we confirm that our PSF-based approach is effective in disentangling blended sources in crowded regions.

We conclude this section remarking that it would have been simply impossible to extract the light curve of TR1 from *Kepler*/K2 data without using a input list from an higher resolution data set and subtracting the stellar neighbours. The approach of our method allows us to reach a 6.5-h photometric precision of ~ 2700 ppm in a heavily crowded environment for sources as faint as TR1.

¹² As suggest by the referee, using EXOFAST tool (Eastman, Gaudi, & Agol 2013) we found an impact parameter of 0.764114 and a “planet” (star in TR1 case) to star radius ratio of 0.184497, confirming our qualitative classification.

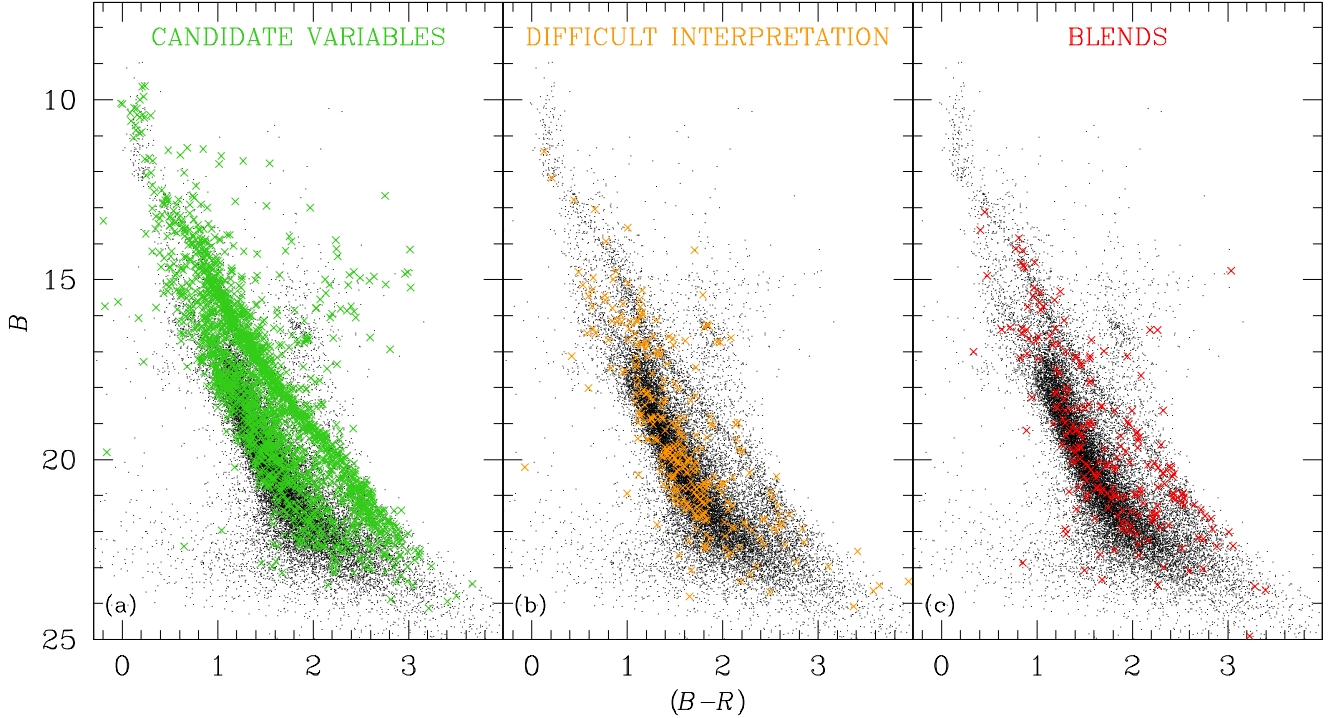


Figure 20. Distribution of our 2849 candidate variables in the B vs. $(B - R)$ CMD. In the three panels we separately show the likely-variable stars (green crosses in panel a), the objects of which the LC was of difficult interpretation (orange crosses in panel b) and the blends (red crosses in panel c).

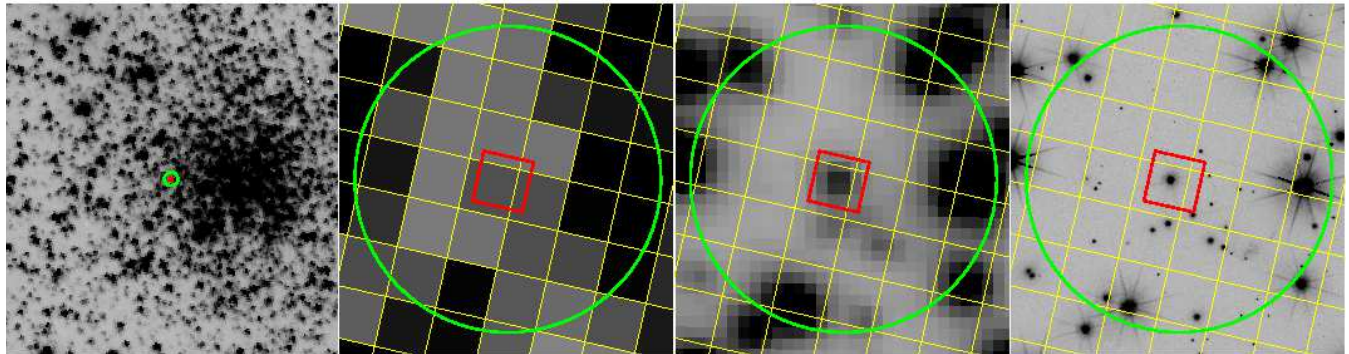


Figure 21. (Left): 10×10 arcmin 2 region around TR1 in the $K2$ stacked image. A green circle of radius 3 $Kepler$ pixels and a red square with 1 $Kepler$ pixel side are centered on TR1. (Middle-left): zoom-in of the $K2$ stacked image around TR1. The covered area is about 6.5×6.8 pixel 2 (about 25×28 arcsec 2). The yellow grid represents the $Kepler$ CCD pixel grid. (Middle-right): as in the Middle-left panel, but for the Schmidt filter-less stacked image of Nardiello et al. (2015). (Right): ACS/WFC@HST F606W-filter stacked image (from Bedin et al. 2010). In all these panels, North is up and East to the left. It is clear that the higher the image resolution, the higher the number of detectable polluting sources within the aperture.

10 ELECTRONIC MATERIAL

For each source in the AIC that fall in a $K2/C0$ /channel-81 TPF, we release raw and detrended light curves from the 1-, 3-, 5-, 10-pixel aperture and PSF photometry on the neighbour-subtracted images. We also make public available the AIC (with each star flagged as in/out any TPF) and the $K2$ stacked image.

For the 2849 candidate variables we release¹³ a catalogue made as follow. Column (1) contains the ID of the star in the AIC. Columns (2) and (3) give J2000.0 equatorial coordinates in deci-

mal degrees; Columns (4) and (5) contain the pixel coordinates x and y from the AIC, respectively. In columns (6) and (7) we release the instrumental Schmidt filter-less and the K_p magnitudes of the stars. The K_p magnitude is computed as the 3σ -clipped median value of the magnitude in the LC, calibrated using a photometric zero-point as described in Sect 5. In column (8) we write the photometric method with which we extracted the LC of the object and searched for variability.

Column (9) contains a flag corresponding to our by-eye classification of the LC (Sect. 8.1 and 8.2):

- 0: high probability that it is a blend;
- 1: candidate variable;

¹³ <http://groups.dfa.unipd.it/ESPG/Kepler-K2.html>

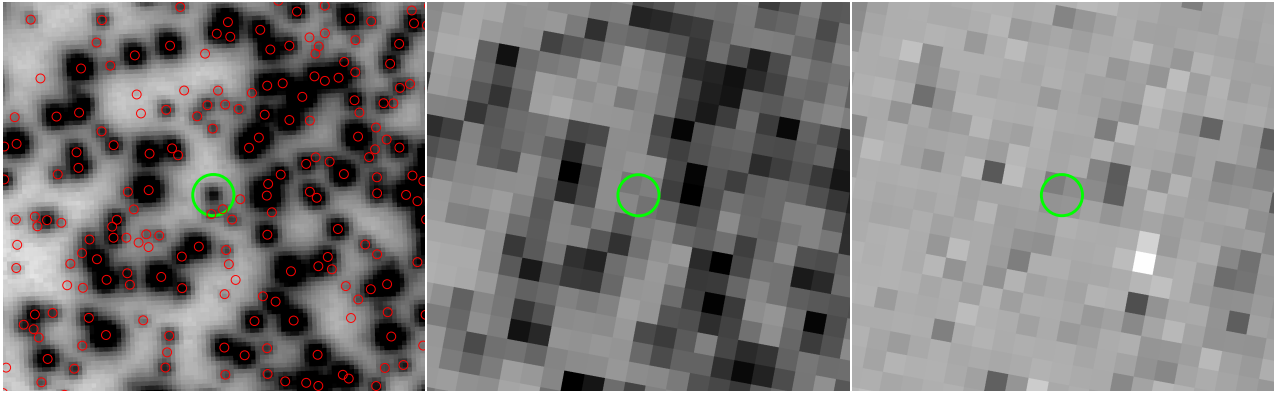


Figure 22. PSF-subtraction of the stellar neighbours (red circles) around TR1 (green circle). In the *Left* panel, we show all identified sources in the AIC that must be subtracted before measuring the TR1 magnitude. The image is the Schmidt stacked image from which the AIC was extracted. In the *Middle* and *Right* panels we show a single *K2* image before and after the neighbour subtraction, respectively. Even if the PSF-based subtraction is not perfect due to the unavailable PSF calibration data (see Sect. 3), the light pollution is less severe.

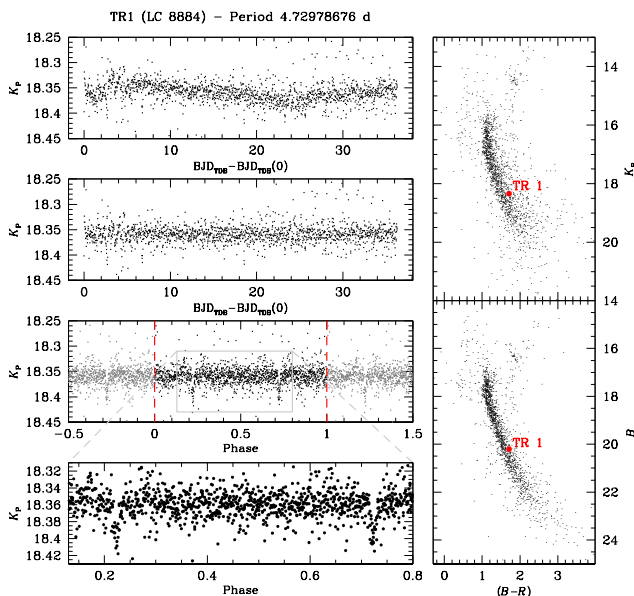


Figure 23. TR1 clean LCs and CMD location. (*Left*): from *Top* to *Bottom*: detrended LC, flattened LC (see text for details), phased LC with a period of 4.72978676 days and zoom-in on the phased LC to highlight the two minima. In the one-to-the-last panel, the red, vertical dashed lines are set at phase 0 and 1. (*Right*): K_p vs. $(B-R)$ (*Top* panel) and B vs. $(B-R)$ (*Bottom* panel) CMDs of NGC 2158. We considered as cluster members those stars that are within a radius of ~ 3 arcmin from NGC 2158 center. The red filled point marks the location of TR1. The K_p magnitude was computed as the 3σ -clipped median value of the PSF-based LC magnitude, calibrated into the *Kepler* photometric system (Sect 5).

- 2: difficult to classify;
- 30: star marked as “difficult to classify” and that, by comparison with the literature, could be a possible blend;
- 31: star marked as “difficult to classify”, but for which we found a correspondence in the literature;
- 32: star we classified as candidate variable but it is close to a variable star from the literature and that seems a possible blend.

Column (10) gives the period, when available. From column (11) to (16) we give the ID used in other published catalogues,

namely Nardiello et al. (2015), Hu et al. (2005), Jeon & Lee (2010), Kim et al. (2004), Meibom, Mathieu, & Stassun (2009), Mocjejska et al. (2004, 2006), respectively. Finally, we provide (columns from 17 to 22) the $BVRJ_{2MASS}H_{2MASS}K_{2MASS}$ calibrated magnitudes from Nardiello et al. (2015) catalogue, when available.

11 CONCLUSIONS AND FUTURE PLANNED WORKS

In this paper we have presented our first analysis of *K2* data, focusing our effort on crowded images and faint stars. The test-beds for our method were super-stamps covering the OCs M 35 and NGC 2158.

Though the lack of *Kepler* calibration data – not made available yet to the community – prevented us to optimize our algorithm, based on a technique we have developed in the last 20 years on *HST* undersampled images, we nevertheless succeeded in implementing a photometric procedure based on the ePSF concept (Anderson & King 2000). We have shown that by using a crude PSF that is spatially constant across the channel and allowing for simple temporal variations, we were able to properly fit stellar objects. Future efforts will be devoted to further improve the PSF model, possibly with a better data set at our disposal.

In the second part of the paper, we focused our attention on the light-curve-extraction method and on the consequent detrending algorithms. The LC extraction is based on the methods we started to develop in Nardiello et al. (2015) and makes use of both PSF fitting and of an high-angular-resolution input list to subtract stellar neighbours before measuring the stellar flux of any given target. By subtracting the light of the close-by stars, we are able to decrease the dilution effects that significantly impact the photometry in crowded regions.

We compared aperture- and PSF-based photometric methods and found that aperture photometry performs better on isolated, bright stars (6.5-hour-rms best value of ~ 30 ppm), while PSF photometry shows a considerable improvement with respect to the classical aperture photometry on faint stars and in crowded regions. The extension of the capability to exploit *Kepler* as well as *K2* data set to fainter (up to 5 magnitudes fainter than what has been done up to now in the literature) stars and crowded environments is the main and original contribution of our efforts.

We release our raw and detrended LCs with the purpose of

stimulating the improvement of variable- and transit-search algorithms, as well as of the detrending methods.

We are currently working on other clusters imaged during other *K2* Campaigns, and plan to work on the densest Galactic-bulge regions. We also plan to go back to open clusters within the *Kepler* field, i.e. NGC 6791 and NGC 6819.

ACKNOWLEDGMENTS

We thank the referee Dr. A. Vanderburg for the careful reading and suggestions that improved the quality of our paper. ML, LRB, DN and GP acknowledge PRIN-INAF 2012 partial funding under the project entitled “The M4 Core Project with Hubble Space Telescope”. DN and GP also acknowledge partial support by the Università degli Studi di Padova Progetto di Ateneo CPDA141214 “Towards understanding complex star formation in Galactic globular clusters”. The authors warmly thank Dr. Jay Anderson for the discussions and improvements to the text. Finally, we thank Dr. B. J. Mochejska for the discussion about TR1.

REFERENCES

Adams F. C., Proszkow E. M., Fatuzzo M., Myers P. C., 2006, *ApJ*, 641, 504

Aigrain S., Hodgkin S. T., Irwin M. J., Lewis J. R., Roberts S. J., 2015, *MNRAS*, 447, 2880

Anderson J., & King, I. R. 2000, *PASP*, 112, 1360

Anderson J., King I. R., 2006, *acs..rept*, 1

Anderson J., Bedin L. R., Piotto G., Yadav R. S., Bellini A., 2006, *A&A*, 454, 1029

Anderson J., et al., 2008, *AJ*, 135, 2114

Armstrong D. J., et al., 2015, *A&A*, 579, A19

Balona L. A., Baran A. S., Daszyńska-Daszkiewicz J., De Cat P., 2015, *MNRAS*, 451, 1445

Barnes S. A., 2007, *ApJ*, 669, 1167

Bedin L. R., Salaris M., King I. R., Piotto G., Anderson J., Cassisi S., 2010, *ApJ*, 708, L32

Bellini A., et al., 2014, *ApJ*, 797, 115

Brogaard K., Bruntt H., Grundahl F., Clausen J. V., Frandsen S., Vandenberg D. A., Bedin L. R., 2011, *A&A*, 525, A2

Brown T. M., Latham D. W., Everett M. E., Esquerdo G. A., 2011, *AJ*, 142, 112

Brucalassi A., et al., 2014, *A&A*, 561, L9

Bryson S. T., et al., 2010, *ApJ*, 713, L97

Crossfield I. J. M., et al., 2015, *ApJ*, 804, 10

Eastman J., Gaudi B. S., Agol E., 2013, *PASP*, 125, 83

Foreman-Mackey D., Montet B. T., Hogg D. W., Morton T. D., Wang D., Schölkopf B., 2015, *ApJ*, 806, 215

Gilliland R. L., et al., 2000, *AAS*, 32, 675

Hartman J. D., Gaudi B. S., Holman M. J., McLeod B. A., Stanek K. Z., Barranco J. A., Pinsonneault M. H., Kalirai J. S., 2008, *ApJ*, 675, 1254

Hartman J. D., et al., 2009, *ApJ*, 695, 336

Hermes J. J., et al., 2015, *MNRAS*, 451, 1701

Howell S. B., et al., 2014, *PASP*, 126, 398

Hu J.-H., Ip W.-H., Zhang X.-B., Jiang Z.-J., Ma J., Zhou X., 2005, *ChJAA*, 5, 356

Huang C. X., Penev K., Hartman J. D., Bakos G. Á., Bhatti W., Domsa I., de Val-Borro M., 2015, *arXiv*, arXiv:1507.07578

Jeon Y.-B., 2010, *PKAS*, 25, 31

Kim H.-J., Park H.-S., Kim S.-L., Jeon Y.-B., Lee H., 2004, *IBVS*, 5558, 1

Koch D. G., et al., 2010, *ApJ*, 713, L79

Kovács G., Zucker S., Mazeh T., 2002, *A&A*, 391, 369

Kraus A. L., Cody A. M., Covey K. R., Rizzuto A. C., Mann A. W., Ireland M. J., 2015, *ApJ*, 807, 3

LaCourse D. M., et al., 2015, *MNRAS*, 452, 3561

Lund M. N., Handberg R., Davies G. R., Chaplin W. J., Jones C. D., 2015, *ApJ*, 806, 30

Mamajek E. E., Hillenbrand L. A., 2008, *ApJ*, 687, 1264

Meibom S., Mathieu R. D., Stassun K. G., 2009, *ApJ*, 695, 679

Meibom S., et al., 2011, *ApJ*, 733, L9

Meibom S., et al., 2013, *Natur*, 499, 55

Meibom S., Barnes S. A., Platais I., Gilliland R. L., Latham D. W., Mathieu R. D., 2015, *Natur*, 517, 589

Mochejska B. J., Stanek K. Z., Sasselov D. D., Szentgyorgyi A. H., Westover M., Winn J. N., 2004, *AJ*, 128, 312

Mochejska B. J., et al., 2006, *AJ*, 131, 1090

Montalto M., et al., 2007, *A&A*, 470, 1137

Nardiello, D., Bedin, L. R., Nascimbeni, V., et al. 2015, *MNRAS*, 447, 3536

Nascimbeni V., Bedin L. R., Piotto G., De Marchi F., Rich R. M., 2012, *A&A*, 541, A144

Pont F., Zucker S., Queloz D., 2006, *MNRAS*, 373, 231

Press W. H., Teukolsky S. A., Vetterling W. T., Flannery B. P., 1992, *nrca.book*

Quinn S. N., et al., 2012, *ApJ*, 756, L33

Quinn S. N., et al., 2014, *ApJ*, 787, 27

Schwarzenberg-Czerny A., 1989, *MNRAS*, 241, 153

Stello D., et al., 2011, *ApJ*, 739, 13

Stello D., et al., 2015, *ApJ*, 809, L3

Vanderburg A., 2014, *arXiv*, arXiv:1412.1827

Vanderburg A., Johnson J. A., 2014, *PASP*, 126, 948

Vanderburg A., et al., 2015, *ApJ*, 800, 59

Weldrake D. T. F., Sackett P. D., Bridges T. J., 2008, *ApJ*, 674, 1117

Zechmeister M., Kürster M., 2009, *A&A*, 496, 577

APPENDIX A: EXAMPLE OF LIGHT CURVES

In this appendix we show 10 of our light curves as example (Fig. A1).

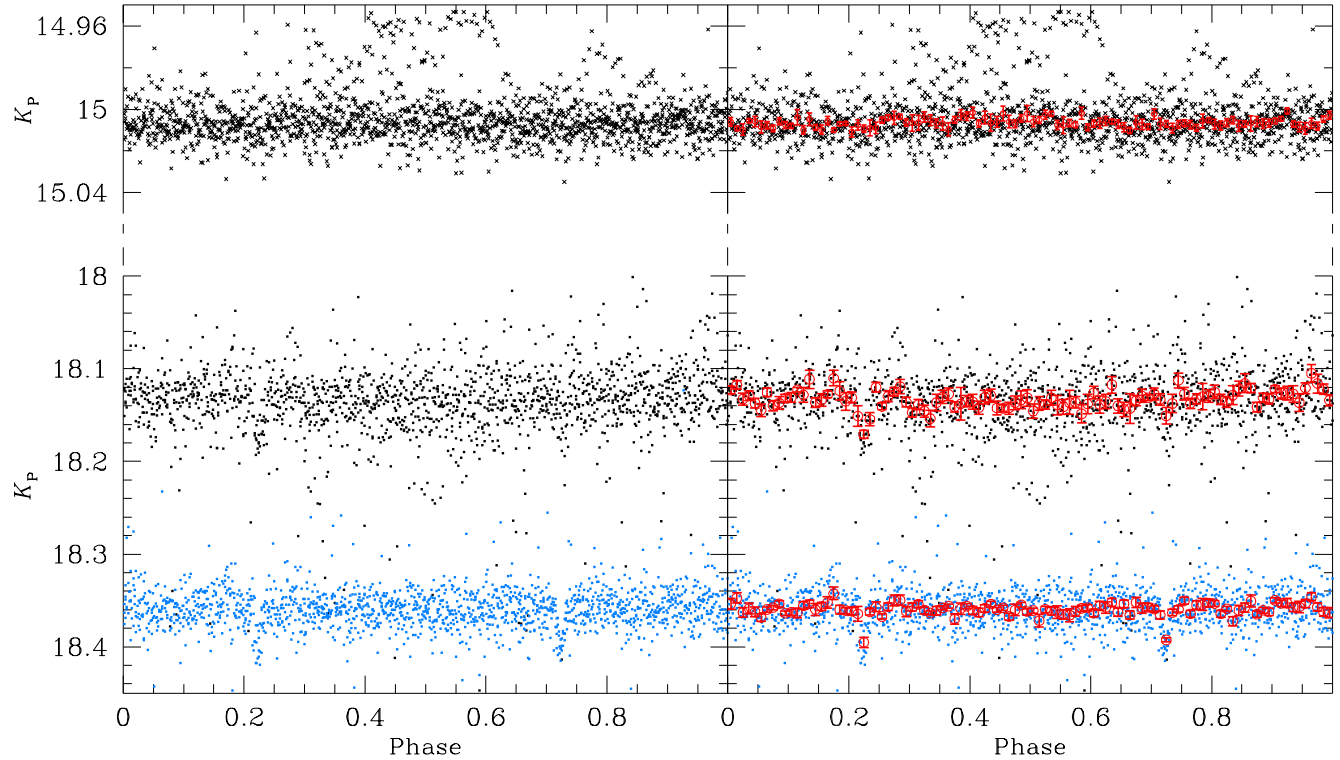


Figure 24. TR1 clean LCs with and without TR1 neighbours. From *Top* to *Bottom*: 3-pixel-aperture LC with neighbours (black crosses), PSF-based LC with (black dots) and without (azure dots) neighbours. The LCs are phased with a period of 4.72978676 d. In the *Right* panels we also plot the binned LCs. The red points are the median value in 0.01-phase bin, while the error bars are the 68.27th percentile of the distribution around the median value divided by \sqrt{N} , where N is the number of points in each bin.

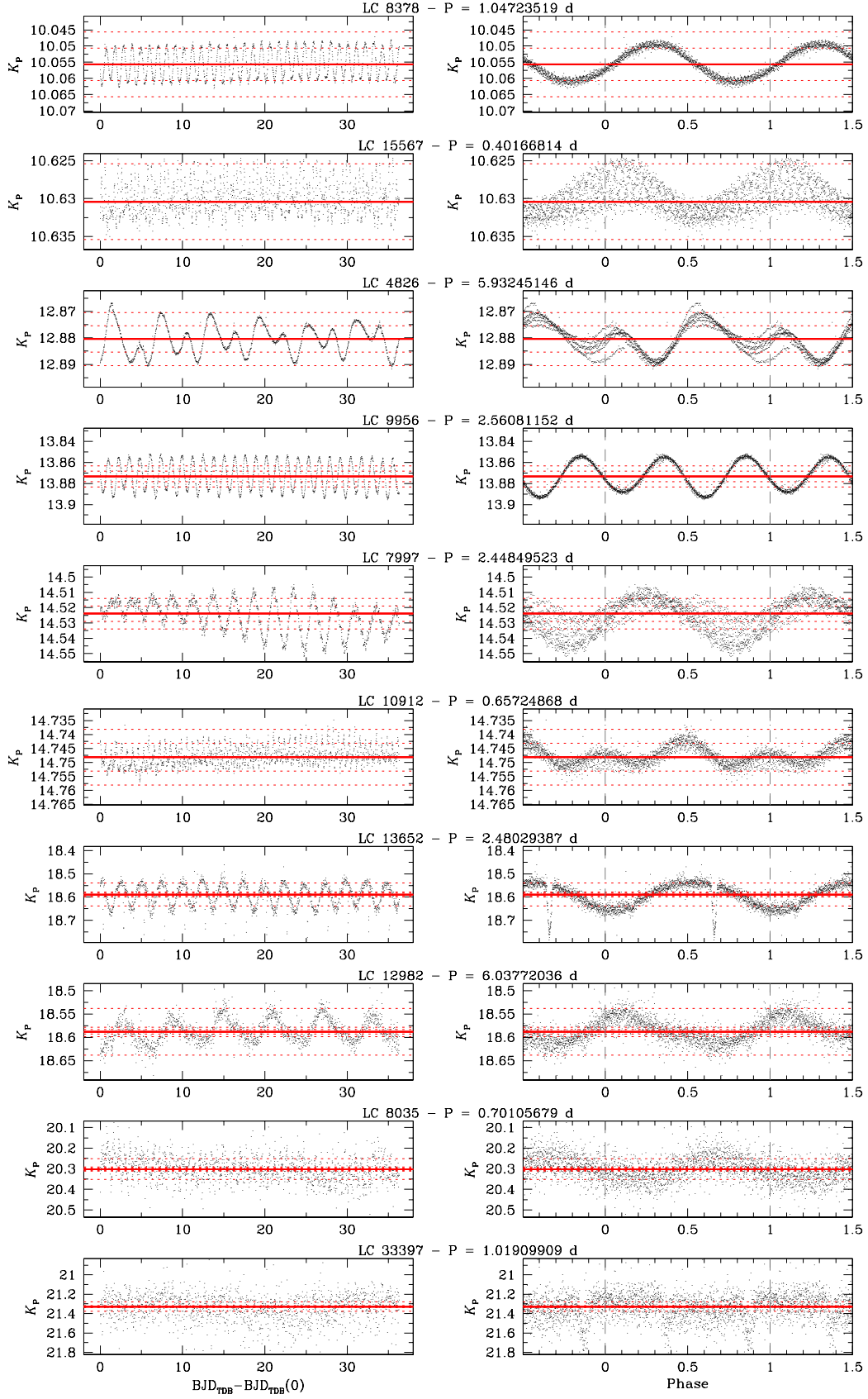


Figure A1. Example of variable light curves in our sample. We plot on the *Left* and on the *Right* the entire and the folded detrended clean LC of each object. The red solid line is set at the median magnitude of the LC, while the red dashed lines are set at ± 0.005 , ± 0.01 and ± 0.05 K_p from the median value. The vertical, gray dashed lines in the *Right* panels are set at phase 0 and 1. The LCs are plotted in order of decreasing magnitude from the top to the bottom.